

Stability of a Cold Core Eddy in the Presence of Convection: Hydrostatic versus Nonhydrostatic Modeling

M. JEROEN MOLEMAKER* AND HENK A. DIJKSTRA

*Department of Physics and Astronomy, Institute for Marine and Atmospheric Research, Utrecht University,
Utrecht, Netherlands*

(Manuscript received 8 October 1997, in final form 8 February 1999)

ABSTRACT

Geostrophic eddies in a stratified liquid are susceptible to baroclinic instabilities. In this paper, the authors consider these instabilities when such an eddy is simultaneously cooled homogeneously from above. As a linear stability analysis shows, the developing convection modifies the background stratification, the stability boundaries, and the patterns of the dominant modes. The coupling between the effects of convection and the large-scale flow development of the eddy is studied through high-resolution numerical simulations, using both nonhydrostatic and hydrostatic models. In the latter models, several forms of convective adjustment are used to model convection. Both types of models confirm the development of the dominant modes and indicate that their nonlinear interaction leads to localized intense convection. By comparing nonhydrostatic and hydrostatic simulations of the flow development carefully, it is shown that convective adjustment may lead to erroneous small-scale variability. A simple alternative formulation of convective adjustment is able to give a substantial improvement.

1. Introduction

The transformation of surface water into intermediate and deep water through deep convection appears to be a very important process in the ocean. It affects the strength of the thermohaline overturning circulation in the Atlantic and hence the meridional heat transport. By now, much is known on the actual scales of convection, the physical processes determining these scales, and the effects of convection on the large-scale flow development. Observations in the Greenland Sea (Schott et al. 1993), in the Labrador Sea (Gascard and Clarke 1983), and in the Mediterranean (Schott and Leaman 1991) indicate that deep convection occurs only at specific sites and is a very localized process both with respect to time and space. Surface cooling and possibly brine rejection by sea ice formation induce vigorous convection in the form of plumes with a horizontal scale of $O(1\text{ km})$, which are organized within larger-scale structures of $O(50\text{ km})$. The mixing of heat and salt induced by the convection and the subsequent geostrophic ad-

justment eventually leads to a large-scale modification of deeper water masses. This interaction between small-scale convection and the larger geostrophic scales is a crucial problem in the parameterization of water mass transformation.

Because of the localized nature of the convection process, a prototype situation of study in the laboratory has been the development of convection in a stratified rotating layer of liquid due to a localized negative surface buoyancy flux (Maxworthy and Narimousa 1994; Coates et al. 1995). In most of the experiments, the liquid is initially at rest and the surface buoyancy flux is confined to a disk with a smaller extent than the total flow domain. During the first stages of flow development, a well-mixed layer grows downward through entrainment and a lateral buoyancy gradient develops. The flow is not influenced by rotation until it reaches the depth at which the Rossby number based on the local velocity and length scale becomes small enough (Coates et al. 1995; Coates and Ivey 1997). In a next stage, geostrophic adjustment on the scale of the cooling disk leads to a rim current along the edge of the convecting area. This rim current subsequently becomes unstable through baroclinic instability. The resulting vortices, having a horizontal scale of the local internal Rossby deformation radius, spread away from the original convective region inducing lateral transports of heat and salt. Eventually, a quasi-steady state may occur in which the energy loss through the surface is balanced by the

* Current affiliation: Institute of Geophysics and Planetary Physics, University of California, Los Angeles, Los Angeles, California.

Corresponding author address: Dr. M. Jeroen Molemaker, Institution for Geophysics and Planetary Physics, University of California, Los Angeles, 405 Hilgard Avenue, Los Angeles, CA 90015.
E-mail: nmolem@atmos.ucla.edu

fluxes through the lateral boundaries of the convective region.

Numerical simulations using nonhydrostatic models (Jones and Marshall 1993; Klinger and Marshall 1995; Send and Marshall 1995; Visbeck et al. 1996) have greatly contributed to the understanding of these flows. Different flow regimes exist, depending on the magnitude of the rotation rate f , the initial stratification measured by the buoyancy frequency N , the surface buoyancy flux B_0 , and the depth of the layer H . A key parameter for the small-scale flow development is the natural Rossby number $Ro^* = B_0^{1/2}/(Hf^{3/2})$, which is the ratio of the characteristic vertical mixing timescale in the rotationally affected regime and the geostrophic adjustment timescale. If Ro^* is large, the developing convection remains essentially three-dimensional, while if Ro^* is small, geostrophic adjustment is relatively fast and the convection is quasi two-dimensional (Klinger and Marshall 1995).

In all of these studies, the initial horizontal scale of the convective region, that is, the radius of the cooling region, is prescribed. In reality, the cooling by the atmosphere is not so strictly localized and one would expect that, depending on the stratification, a much larger region would overturn (Killworth 1983). To explain why the process is so localized it has been suggested that topography (Alverson and Owens 1996) or horizontal gradients in the background density field (Maded et al. 1996) limits the sites of convective activity. Doming of isopycnal surfaces due to the large-scale cyclonic background flow has been observed in the Greenland Sea (Gascard and Clarke 1983) and in the Mediterranean (Schott and Leaman 1991). While this large-scale preconditioning of the density field may add to the occurrence of convection, it still does not explain its spatially localized nature.

The localization of convection through the presence of cold core eddies was suggested by Johannessen et al. (1991) based on observations in the northern Greenland Sea. Typical horizontal scales of these eddies were 10 km and a typical eddy lifetime was about 20–30 days. The majority of these eddies rotated cyclonically with orbital speeds of around 20 cm s⁻¹. In a recent study, Legg et al. (1998) studied a prototype problem of this localization by studying numerically the flow development of a cold core eddy that was cooled homogeneously from above. Very localized convection can indeed occur due to the presence of such an eddy. The structure of the eddy determines the initial stratification with a buoyancy frequency varying both as a function of distance to the eddy center as well as with depth. The mixed layer deepening through convection is therefore inhomogeneous and leads to a restratification in the eddy region. After this restratification, smaller eddies develop along the edge of the original eddy through baroclinic instabilities, which eventually leads to break-up into multiple eddies.

The baroclinic instability process is an essential fea-

ture in the large-scale flow development. The instability of an eddy has been studied in a laboratory experiment by Saunders (1973) and Griffiths and Linden (1981). In both studies it was found that the stability of the eddy crucially depends on the Burger number $Bu = (L_\rho/R_0)^2$, the square of the ratio of the internal Rossby deformation radius $L_\rho = NH/f$, and a characteristic horizontal length scale of the eddy, that is, the initial eddy radius R_0 . A necessary condition for baroclinic instability of a two-layer quasigeostrophic vortex is that $Bu < 1/4$ (Pedlosky 1985).

Although their initial (standard) eddy is more complicated, Legg et al. (1998) mention that this cold core eddy is stable to small perturbations in the absence of cooling. Cooling decreases L_ρ and therefore increases the ratio R_0/L_ρ since R_0 is fixed, which eventually gives conditions under which the eddy becomes unstable. Legg et al. (1998) calculate the growth rate σ of the baroclinic perturbations from the numerical simulations and find that it compares well with the classical growth rates in the Eady problem (Eady 1949), which scale as

$$\sigma = \frac{f}{N} \frac{\partial v}{\partial z}$$

v being the meridional velocity of the initial eddy. However, they were not able to estimate the scale of the patterns of the instability and its dependence on the initial eddy size and strength.

The baroclinic instability process of the eddy is of major importance to the lateral exchange and therefore of the long time modification of the water masses involved. In this paper, we consider the baroclinic instability problem of cold-core eddies in more detail, by solving the linear stability problem within the full 3D nonhydrostatic model formulated in section 2. In section 3, the linear stability of geostrophic eddies is calculated. The effect of convection is modeled through its modification of the surface stratification. We calculate the patterns and growth rates of the most unstable perturbations for different eddy sizes. Subsequently, a high resolution numerical simulation using a 3D nonhydrostatic model is performed and the time and space scales found are compared to those predicted by the linear stability analysis (section 4).

Recently, several studies have been carried out on shallow convection in an idealized coastal polynia (Gawarkiewicz and Chapman 1995; Chapman and Gawarkiewicz 1997). In section 5, the same flow is simulated using a hydrostatic model with a resolution that resolves the baroclinic eddy scale. The effects of convection on the mixing of buoyancy is parameterized using convective adjustment. Considering the criteria developed in Marshall et al. (1997a), the large-scale flow development of the cooled geostrophic eddies is certainly in the hydrostatic regime. However, since our linear stability results imply that the growth rate of the baroclinic instabilities is strongly modified by convection, one may

ask whether the correct large-scale flow development is obtained when convection is represented in a hydrostatic model by convective adjustment. This representation issue of convection is studied in section 5 and both the linear stability results and the high resolution nonhydrostatic simulation serve as a reference case for the results obtained with course resolution hydrostatic simulations.

2. Formulation

a. Model

Consider a liquid with (eddy) viscosity κ_m and thermal diffusivity κ_T in a rotating rectangular domain of length L_x , width L_y , and height H . At the top of the liquid, a constant negative buoyancy flux B_0 is prescribed through a constant heat flux \mathcal{H} , which cools the layer homogeneously from above. With the velocity vector \mathbf{u} , the pressure p , the temperature T and the density ρ , the governing equations (using the Boussinesq approximation) describing the deviation from hydrostatic equilibrium are given by

$$\frac{\partial \mathbf{u}}{\partial t} + \mathbf{u} \cdot \nabla \mathbf{u} + f \mathbf{e}_3 \times \mathbf{u} = -\frac{1}{\rho_0} \nabla p + \nabla \cdot (\kappa_m \nabla \mathbf{u}) - \mathbf{e}_3 \frac{g\rho}{\rho_0} \tag{1a}$$

$$\nabla \cdot \mathbf{u} = 0 \tag{1b}$$

$$\rho = -\rho_0 \alpha T \tag{1c}$$

$$\frac{\partial T}{\partial t} + \mathbf{u} \cdot \nabla T = \nabla \cdot (\kappa_T \nabla T), \tag{1d}$$

where f is the Coriolis parameter, α is the thermal compressibility, and \mathbf{e}_3 the unit vector in the vertical direction. Both the viscosity and the thermal diffusivity are assumed constant and equal to κ . The governing equations are nondimensionalized using scales H , κ/H , $\rho_0 \kappa^2/H^2$, H^2/κ , and $\rho_0 H B_0 / (\kappa g)$ for length, velocity, pressure, time, and density, respectively, such that the total dimensional density ρ^* is calculated from the dimensionless ρ by $\rho^* = \rho_0 [1 + H B_0 \rho / (\kappa g)]$. This leads to the following nondimensional equations:

$$\frac{\partial \mathbf{u}}{\partial t} + \mathbf{u} \cdot \nabla \mathbf{u} + \sqrt{\text{Ta}} \mathbf{e}_3 \times \mathbf{u} = -\nabla p + \nabla^2 \mathbf{u} - \mathbf{e}_3 \text{Ra} \rho \tag{2a}$$

$$\nabla \cdot \mathbf{u} = 0 \tag{2b}$$

$$\frac{\partial \rho}{\partial t} + \mathbf{u} \cdot \nabla \rho = \nabla^2 \rho, \tag{2c}$$

where the temperature has been eliminated using (1c). The domain is assumed periodic in the horizontal. The top boundary is assumed to be stress free while the bottom satisfies no-slip conditions. The bottom boundary satisfies a no-flux condition for the density while a

constant density flux is prescribed at the top. The dimensionless boundary conditions at top and bottom are

$$z = 1: \quad \frac{\partial \rho}{\partial z} = 1; \quad \frac{\partial u}{\partial z} = 0; \quad \frac{\partial v}{\partial z} = 0; \quad w = 0 \tag{3a}$$

$$z = 0: \quad \frac{\partial \rho}{\partial z} = 0; \quad u = 0; \quad v = 0; \quad w = 0. \tag{3b}$$

Apart from the two aspect ratios $A_x = L_x/H$ and $A_y = L_y/H$ of the basin, two other dimensionless parameters appear, the Taylor number Ta and the flux Rayleigh number Ra , which are given by

$$\text{Ra} = \frac{H^4 B_0}{\kappa^3}, \quad \text{Ta} = \frac{H^4 f^2}{\kappa^2}. \tag{4}$$

b. Cold core eddies in geostrophic balance

Our aim is to determine the influence of convection on the large-scale linear stability of cold core eddies. To define such eddies, we first write the equations (2) in polar coordinates (r, θ, z) with radial velocity u , azimuthal velocity v , and vertical velocity w ; that is,

$$\frac{\partial u}{\partial t} + \mathbf{u} \cdot \nabla u - \frac{v^2}{r} - \sqrt{\text{Ta}} v = -\frac{\partial p}{\partial r} + \nabla^2 u - \frac{u}{r^2} - \frac{2}{r^2} \frac{\partial v}{\partial \theta} \tag{5a}$$

$$\frac{\partial v}{\partial t} + \mathbf{u} \cdot \nabla v + \frac{uv}{r} + \sqrt{\text{Ta}} u = -\frac{1}{r} \frac{\partial p}{\partial \theta} + \nabla^2 v + \frac{2}{r^2} \frac{\partial u}{\partial \theta} - \frac{v}{r^2} \tag{5b}$$

$$\frac{\partial w}{\partial t} + \mathbf{u} \cdot \nabla w = -\frac{\partial p}{\partial z} + \nabla^2 w - \text{Ra} \rho \tag{5c}$$

$$\frac{1}{r} \frac{\partial}{\partial r}(ru) + \frac{1}{r} \frac{\partial v}{\partial \theta} + \frac{\partial w}{\partial z} = 0 \tag{5d}$$

$$\frac{\partial \rho}{\partial t} + \mathbf{u} \cdot \nabla \rho = \nabla^2 \rho \tag{5e}$$

with

$$\mathbf{u} \cdot \nabla = u \frac{\partial}{\partial r} + \frac{v}{r} \frac{\partial}{\partial \theta} + w \frac{\partial}{\partial z};$$

$$\nabla^2 = \frac{1}{r} \frac{\partial}{\partial r} \left(r \frac{\partial}{\partial r} \right) + \frac{1}{r^2} \frac{\partial^2}{\partial \theta^2} + \frac{\partial^2}{\partial z^2}$$

and with the boundary conditions (3) at top and bottom.

Steady parallel flow solutions $\bar{u} = 0$, $\bar{v}(r, z)$, $\bar{w} = 0$, $\bar{\rho}(r, z)$ are not easily found analytically. Hence, a procedure is needed to find approximate parallel flow solutions. First, a background density field is defined by

TABLE 1. Standard values of the dimensional and dimensionless parameters.

Dimensional parameter	Value
H	10^3 m
L_x	32×10^3 m
L_y	32×10^3 m
B_0	10^{-7} m ² s ⁻³
κ	10^{-1} m ² s ⁻¹
f	10^{-4} s ⁻¹
\mathcal{H}	200 W m ⁻²
α	10^{-4} K ⁻¹
Dimensionless parameter	Value
A_x	32
A_y	32
Ra	10^8
Ta	2×10^6
α_e	0.04
γ	3.0
γ_e	4.0
A_e	0.6

$$\bar{\rho}_b(z) = -e^{\gamma(z-1)}, \quad (6)$$

where γ measures the vertical density gradient. This defines a dimensional buoyancy frequency $\bar{N}^2(z) = [\gamma B_0/\kappa]e^{\gamma(z-1)}$ with a maximum at the surface. In Legg et al. (1998), a velocity field $[0, \bar{v}(r, z), 0]$ is chosen corresponding to a cyclonic (cold core) eddy and the induced dynamic density field is calculated using (5a) and (5c) in the limit of zero friction. In this limit the density field satisfies the steady equation (5e).

Our approach is slightly different, because we want to choose the density field a priori (and later on modify it by including effects of cooling) and calculate the resulting velocity field from this density field. In absence of cooling, the dynamic density field of the eddy that is superposed on the background stratification is chosen as

$$\bar{\rho}_e(r, z) = A_e e^{-\alpha_e r^2} e^{\gamma_e(z-1)}, \quad (7)$$

where A_e is the amplitude of the eddy, α_e controls its horizontal scale, and γ_e defines the vertical decay scale of the eddy. As in the basic state in Legg et al. (1998), also the total density field $\bar{\rho} = \bar{\rho}_e + \bar{\rho}_b$ satisfies the steady equation (5e) in the limit of zero friction. To obtain the flow $\bar{v}_e(r, z)$, which is in geostrophic balance with the density field $\bar{\rho}$, we use the thermal wind relation, neglecting the cyclostrophic term v^2/r in (5a), to give

$$\bar{v}_e(r, z) = -\frac{\text{Ra}}{\sqrt{\text{Ta}}} \int_0^z \frac{\partial \bar{\rho}}{\partial r} dz. \quad (8)$$

For the values of parameters as in Table 1, a vertical slice of the total density distribution $\bar{\rho}$ for $y = A_y/2$ is plotted in Fig. 1a. This figure and following similar figures are plotted using rectangular coordinates where x is given by $x = 0.5A_x + r \cos\theta$. The stratification due to the background density field is maximal near the surface, with a maximum value corresponding to $\bar{N}^2 =$

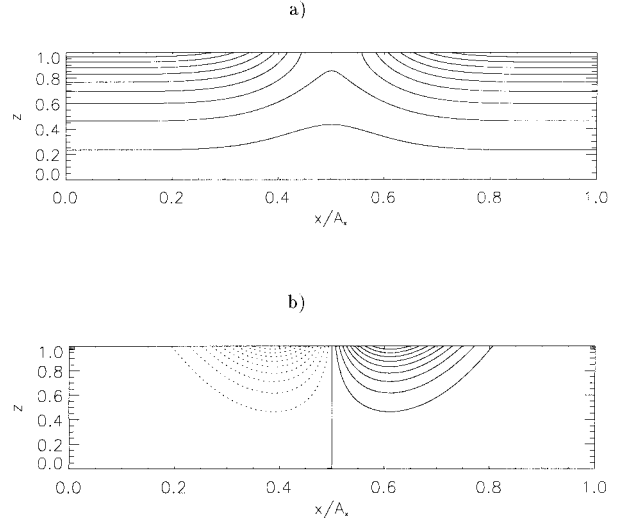


FIG. 1. (a) Contour plot of the density field $\bar{\rho}$ for a vertical slice at $y = 0.5A_y$. The contour interval is 0.1, corresponding to a buoyancy difference of 10^{-4} m s⁻². (b) Similar plot of the meridional velocity field $\bar{v}_e \cos\theta$ scaled with its maximum value (0.24 m s⁻¹). Solid (dotted) lines indicate positive (negative) velocities, the contour interval is 0.1.

3.0×10^{-6} s⁻². The presence of the geostrophic cyclonic eddy is clearly seen by the doming of the isopycnals near the center of the domain, which coincides with the center of the eddy. The eddy reduces the background density gradient. At the center of the eddy, the resulting density gradient is nearly neutral. The geostrophic meridional velocity of the eddy is shown in Fig. 1b with amplitudes of $O(10^{-1}$ m s⁻¹).

Our procedure of calculating the basic state enables us to take the effect of cooling into account. Starting from the initial density field $\bar{\rho} = \bar{\rho}_e + \bar{\rho}_b$ we determine the density profile $\bar{\rho}_c$ that results if the layer is cooled for 4 hours using the prescribed buoyancy flux $B_0 = 10^{-7}$ m² s⁻³. Here, it is assumed that cooling from the surface leads to a mixed layer with a density that is equal to the density directly underneath the mixed layer at every location. The resulting density profile ρ_c is shown in Fig. 2 in which the mixed layer is shaded. Since the original stratification in the center of the eddy is much weaker than the far-field stratification, the resulting mixed layer is much deeper in the eddy center. Although any adaption of the density profile occurs only

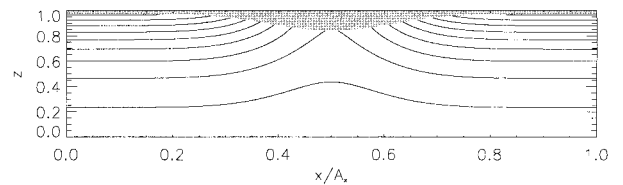


FIG. 2. Contour plot of the density field $\bar{\rho}_c$, which results after 4 hours of cooling of the density profile in Fig. 2a with the buoyancy flux B_0 . Scale and contour intervals as in Fig. 1a.

in the upper part of the domain, it may be important since it erodes the very strong stable density gradients near the surface and therefore destabilizes the eddy. For the density profile $\bar{\rho}_c$, the geostrophic velocity field \bar{v}_c was recalculated through the thermal wind relations. This velocity field hardly differs from \bar{v}_e presented in Fig. 1b and is therefore not shown. The choice of 4 hours as a period over which to cool is rather arbitrary. It is chosen to be large enough for a surface mixed layer to develop, but small enough to limit the modification of the original eddy to the removal of stable density gradients near the surface.

Subsequently, a ‘‘homotopy’’ parameter τ is introduced to ‘‘deform’’ the original basic state corresponding to $\tau = 0$ to the ‘‘cooled’’ basic state corresponding to $\tau = 1$ and a series of basic states is described by

$$\bar{v}(r, z; \tau) = (1 - \tau)\bar{v}_e(r, z) + \tau\bar{v}_c(r, z) \quad (9a)$$

$$\bar{\rho}(r, z; \tau) = (1 - \tau)(\bar{\rho}_b(z) + \bar{\rho}_e(r, z)) + \tau\bar{\rho}_c(r, z). \quad (9b)$$

These basic states will be used for a linear stability analysis in the next section. The density field for $\tau = 0$ corresponds to that shown in Fig. 1, whereas that for $\tau = 1$ is shown in Fig. 2. The velocity field \bar{v} is formally only a steady solution of the inviscid zonal momentum equations in the limit $Ta \rightarrow \infty$ (while keeping Ra/\sqrt{Ta} finite), that is, in the limit of fast rotation. As it is determined here, the velocity field \bar{v} is in exact geostrophic and hydrostatic balance but it does not satisfy the inviscid steady radial momentum equation since the cyclostrophic term is neglected. For the actual parameters used (Table 1), the cyclostrophic term can be calculated from this solution and its maximum for $\tau = 0$ appears to be at most 10% of the geostrophic term.

3. Linear stability analysis

In many studies, standard baroclinic instability theory (Eady 1949) has been applied to obtain the dominant scales associated with the growth of the baroclinic modes. However, this theory is based on a stability analysis of a zonal jet with constant vertical shear and the nonparallel flow associated with a geostrophic eddy may have totally different stability properties.

a. The eigenvalue problem and its solution

To study the stability of the basic states given by (9), infinitesimally small perturbations are considered such that

$$\begin{aligned} (u, v, w, p, \rho)(r, \theta, z, t) \\ = (0, \bar{v}, 0, \bar{p}, \bar{\rho})(r, z) + e^{\sigma t + im\theta}(\hat{u}, \hat{v}, \hat{w}, \hat{p}, \hat{\rho})(r, z), \end{aligned} \quad (10)$$

where $(\hat{u}, \hat{v}, \hat{w}, \hat{p}, \hat{\rho})$ are (complex) functions, m is the azimuthal wavenumber of the perturbations and σ is the complex growth factor. Substitution of (10) into the

equations (5) and linearizing in the perturbation amplitude gives the eigenvalue problem

$$\begin{aligned} \sigma\hat{u} = -\frac{\bar{v}}{r}im\hat{u} + 2\frac{\bar{v}\hat{v}}{r} + \sqrt{Ta}\hat{v} - \frac{\partial\hat{p}}{\partial r} \\ + \nabla^2\hat{u} - \frac{\hat{u}}{r^2} - \frac{2}{r^2}\frac{\partial\hat{v}}{\partial\theta} \end{aligned} \quad (11a)$$

$$\begin{aligned} \sigma\hat{v} = -\hat{u}\frac{\partial\bar{v}}{\partial r} - \frac{\bar{v}}{r}im\hat{v} - \hat{w}\frac{\partial\bar{v}}{\partial z} - \frac{v\hat{u}}{u} - \sqrt{Ta}\hat{u} - \frac{im\hat{p}}{r} \\ + \nabla^2\bar{v} + \frac{2}{r^2}\frac{\partial\hat{u}}{\partial\theta} - \frac{\hat{v}}{r^2} \end{aligned} \quad (11b)$$

$$\sigma\hat{w} = -\frac{\bar{v}}{r}im\hat{w} - \frac{\partial\hat{p}}{\partial z} + \nabla^2\hat{w} - Ra\hat{\rho} \quad (11c)$$

$$0 = \frac{1}{r}\frac{\partial}{\partial r}(r\hat{u}) + \frac{1}{r}im\hat{v} + \frac{\partial\hat{w}}{\partial z} \quad (11d)$$

$$\sigma\hat{\rho} = -\hat{u}\frac{\partial\bar{\rho}}{\partial r} + \frac{\bar{v}}{r}im\hat{\rho} - \hat{w}\frac{\partial\bar{\rho}}{\partial z} + \nabla^2\hat{\rho}, \quad (11e)$$

where

$$\nabla^2 = \frac{1}{r}\frac{\partial}{\partial r}\left(r\frac{\partial}{\partial r}\right) - \frac{m^2}{r^2} + \frac{\partial^2}{\partial z^2}.$$

Together with the homogeneous boundary conditions (3) for the perturbation quantities and boundedness of all perturbation fields for $r \rightarrow \infty$, the problem (11) is an elliptic eigenvalue problem with eigenvalue $\sigma = \sigma_r + i\sigma_i$ and parameters (Ta, Ra, m) in addition to those parameters appearing in the basic state, such as the eddy strength.

To solve this elliptic eigenvalue numerically, first the domain $[0, \infty)$ is transformed into the domain $[0, 1]$ using the mapping

$$r = \frac{\zeta r'}{1 - r'}, \quad (12)$$

where $\zeta = 0.1$. The transformed problem is discretized using second-order finite differences and the (discretized) algebraic eigenvalue problem (11) can be written as

$$\mathbf{Ax} = \sigma\mathbf{Bx}, \quad (13)$$

where \mathbf{x} is the discretized state-variable vector and matrix \mathbf{A} contains the discretized right-hand side of (11). The diagonal matrix \mathbf{B} is singular due to the continuity equation (11d) and the boundary conditions.

The code to calculate the eigenvalues and eigenvectors was verified by considering the classical problem of the differentially heated rotating annulus (Hide and Mason 1975). In this problem, a rotating fluid between two concentric cylinders is subjected to a radial temperature gradient T_r . The parallel basic-state flow is susceptible to baroclinic instability and the relation between the azimuthal wavenumber of the most unstable baroclinic mode and the control parameters Ta and T_r is well

known from experiments (Hide and Mason 1975) and theory. This relation [Fig. 7 in Hide and Mason (1975)] could be reproduced very well with our code. It turned out that for the calculation of the baroclinic stability of the eddies that are considered, a resolution of 64×32 grid points in the (r, z) plane proved to be adequate.

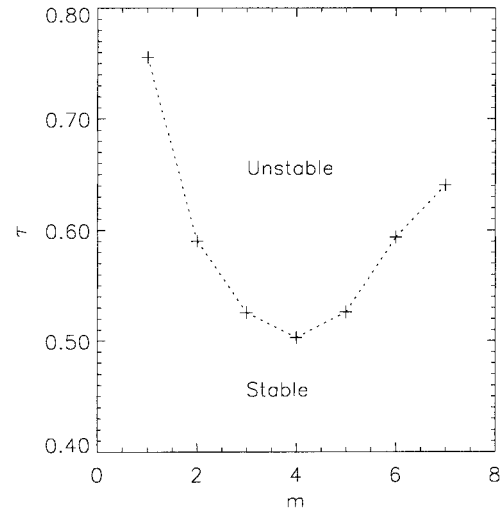
b. Results

The parameters for the standard case are shown in Table 1 and represent a typical situation in the Greenland Sea (Schott et al. 1993). Of course, the background eddy diffusivity κ is quite unsure and chosen as small as possible and still be able to perform the high-resolution numerical simulations in the next section. To be compatible with these simulations, the same value is considered in the linear stability analysis.

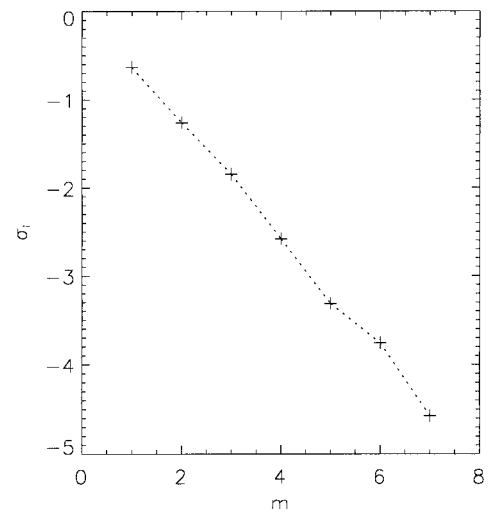
In Fig. 3, the neutral curve in the (m, τ) plane is shown in panel (a) whereas the angular frequencies σ_i are presented in panel (b). For $\tau = 0$, which corresponds to the basic state unmodified through cooling at the surface, the eddy is linearly stable. At $\tau = 0.503$, the basic state becomes unstable to a disturbance having an azimuthal wavenumber $m = 4$. The angular frequencies are negative, indicating cyclonic propagation of disturbances, that is, in the same direction as the basic state. The angular frequencies increase linearly with azimuthal mode number and correspond with a propagation velocity that is nearly constant for every mode number.

A horizontal slice of the vertical velocity of the critical $m = 4$ mode is shown in Fig. 4a. The corresponding density perturbation of the most unstable mode in Fig. 4b has a similar structure as the vertical velocity pattern but it is slightly displaced. Note that these plots only show a snapshot of a propagating mode at a particular phase of the oscillation. In regions of positive vertical velocity, heat is transported downward leading to cooler surface water and hence a positive density perturbation. This density perturbation occurs slightly downstream from locations where positive density anomalies were at an earlier time and hence the perturbation propagates downstream. The slices at $y/A_y = 0.5$ of both fields indicate the strong localization of the perturbation in the region of maximum vertical shear of the basic state near $R_0 = 1/\sqrt{2\alpha_e}$ (at $x = 0.5A_x \pm R_0$ in the figure), with larger amplitude at the center side of this location.

The location of maximal shear of the basic state defines the (dimensionless) wavelength λ and meridional phase speed V of the perturbations, which are given by $\lambda = 2\pi R_0/m$ and $V = R_0\sigma_i/m$. The phase speed of perturbations is slightly higher than the maximum azimuthal velocity of the eddy, in the downstream direction, and its magnitude is about 20 cm s^{-1} . This is larger than the vertically averaged velocity of the basic state, which is the propagation velocity in the standard Eady problem. To compare more closely to the Eady problem, the dependence of the growth factors on the scale of the eddy, determined by α_e , is shown in Fig. 5a for



(a)



(b)

FIG. 3. (a) Neutral curve in the (m, τ) plane where m is the azimuthal mode number and τ controls the shape of the basic state. (b) Angular frequency of the neutral modes in (a).

$\tau = 1$. The case considered above (with $\alpha_e = 0.04$) is shown as the solid curve and shows a maximum growth rate at $m = 4$. Clearly, the mode number m of maximum growth increases with increasing eddy size. For $\alpha_e = 0.01$, the maximum growth rate occurs for $m^* = 14$ while for $\alpha_e = 0.05$ it occurs for $m^* \approx 3$. Smaller eddies have in this case larger growth rates of perturbations, which is not surprising since the gradients from which the perturbations feed are stronger. The range of azimuthal scales of the perturbations shows a cutoff for large m . However, as is evident from Fig. 5 for large m the eddy may become susceptible to other types of instabilities, such as shear instabilities. For example, the second peak in growth rate at $m = 9$ for $\alpha_e = 0.02$ is associated with a vertical shear instability. This can be

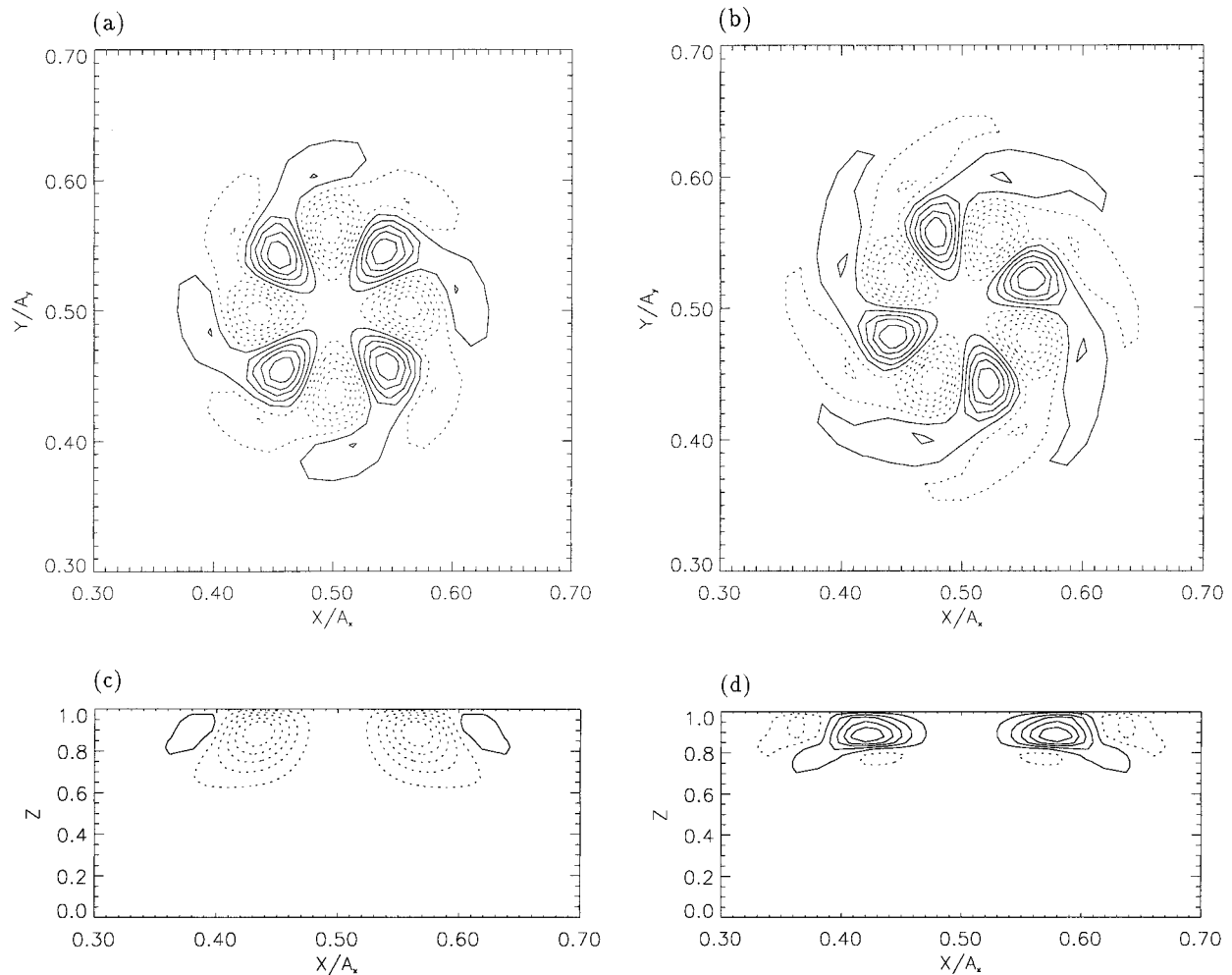


FIG. 4. (a) Vertical velocity distribution of the most unstable perturbation at $z = 0.95$. (b) Density distribution of the most unstable perturbation at $z = 0.95$. (c) Vertical velocity distribution of the most unstable perturbation at $y/A_y = 0.5$. (d) Density distribution of the most unstable perturbation at $y/A_y = 0.5$.

seen from the structure of the mode (not shown) that is markedly different from those shown in Fig. 4. This mode does not have the tail-like structures as in Fig. 4 and its vertical structure reaches much deeper, containing extra nodes. A complete investigation of all possible instabilities on the basic-state eddy would require an extensive investigation that is outside the scope of this paper. Different cooling times to calculate the basic state for $\tau = 0$ are not expected to change the result significantly as long as they are short enough to limit the effects of cooling to the density gradients in the surface layer. The only obvious difference is that for shorter cooling times the eddy will be more stable, but the same modes are expected to dominate.

Eady theory indicates a maximum growth rate for perturbations that have a length-scale about four times the deformation radius L_ρ . In Fig. 6, the value of m^* is plotted as a function of R_0 , showing a near-linear relationship. For each value of α_e , the azimuthal wave-

number adjusts to fit a number of wavelengths of scale L_ρ on the circumference $2\pi R_0$ at the radius of maximum shear. The proportionality constant between m^* and R_0 can be computed from the slope in Fig. 6. It follows that, measured at the radius of maximum shear, the most unstable perturbations have a wavelength of about 5.5 km for the eddy scales considered.

It is well known that the spatial scale of the fastest growing disturbance scales with the Rossby deformation radius L_ρ . However, in this situation, it is not an easy task to define an appropriate L_ρ since it varies strongly over the field. A local density gradient is likely not representative for the whole domain in which the perturbations grow, although it provides small values of L_ρ when convection erodes the surface stratification. A nonlocal estimate of L_ρ can, for example, be obtained through the density difference g' between surface and bottom. This leads to an estimate of L_ρ of

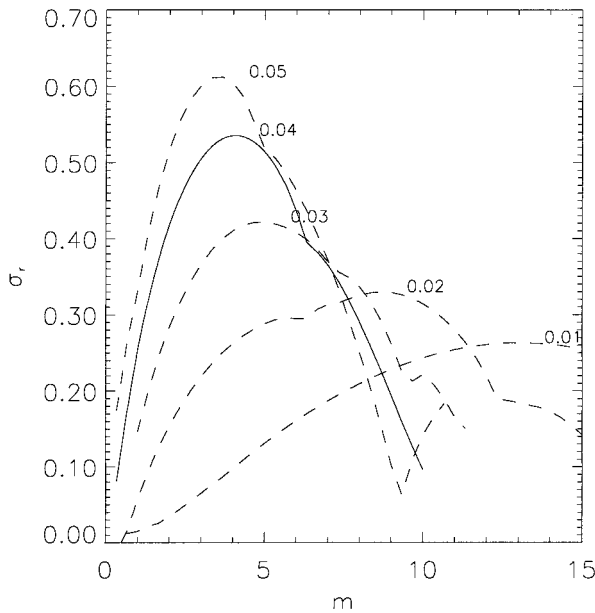


FIG. 5. Growth factor σ_r of the fastest growing modes as a function of azimuthal mode number m for $\tau = 1.0$ (all other parameters as in Table 1). Different curves are for different eddy scale parameters α_e and the solid curve is for $\alpha_e = 0.04$.

$$L_p = \frac{\sqrt{g'H}}{f} = \frac{\sqrt{g(\rho_{\text{sur}} - \rho_{\text{bot}})/\rho_0}H}{f}, \quad (14)$$

which increases from 3.2 km at the center of the eddy to 7.1 km of the background stratification. Another alternative is to estimate L_p from the (surface) density difference between the center of the eddy and the background field. This would lead to an estimate of the Rossby deformation radius of 6.4 km. Both estimates give a value of L_p that is too large to comply with standard Eady theory. Another possibility is to use a volume averaged value for the buoyancy frequency N_{ave} , leading to an integral scale for L_p . We may use Fig. 4 to determine the volume where the perturbation has substantial amplitude and average the buoyancy frequency N over that volume to obtain N_{ave} . The boundaries of such a volume are by no means clearly defined, whereas the resulting values of N_{ave} depend strongly on these. However, if we choose the boundaries of this volume as $x/A_x = [0.5, 0.65]$, $z = [0.8, 1]$ a value of $N_{\text{ave}} = 2.9 \times 10^{-4} \text{ s}^{-1}$ results, corresponding to a much smaller value of $L_p = 2.1 \text{ km}$. This estimate of L_p is much closer to the value expected from standard Eady theory. However, as it is not clear whether the behavior of the growth rates of the perturbations is similar to that in Eady theory, the particular relevant L_p remains unclear.

4. Numerical simulations: Nonhydrostatic model

As a next step toward understanding the impact of convection on the large-scale flow development, a high-resolution simulation was performed using the nonhy-

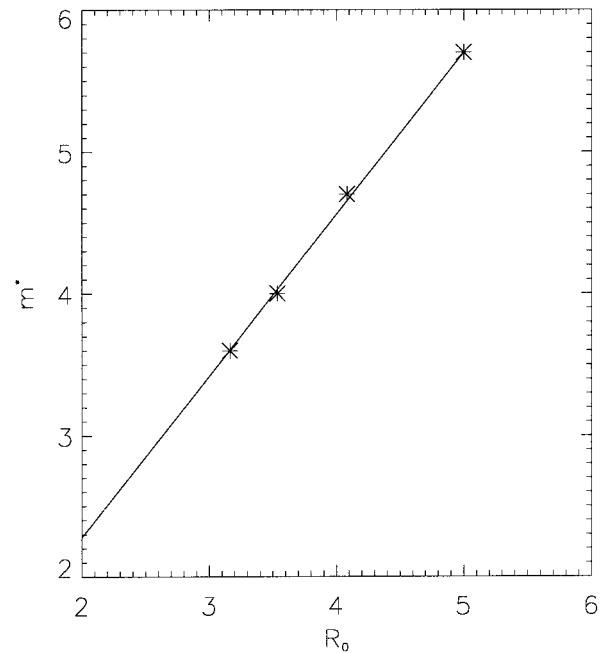


FIG. 6. Most unstable azimuthal wavenumber m^* as a function of the radius of maximal shear R_0 of the eddy.

drostatic model as described in the appendix. The domain is a $32 \times 32 \times 1 \text{ km}^3$ rectangular box and the initial conditions are exactly the basic state (9) for $\tau = 0$.

As a first check on the linear stability results, a simulation was performed at a resolution $256 \times 256 \times 32$, corresponding to $\Delta x = \Delta y = 125 \text{ m}$, $\Delta z = 30 \text{ m}$, of the flow development of the eddy without surface cooling. The flow decays to zero in this case, and the eddy is stable, just as predicted by the linear stability results for $\tau = 0$. It appears that the density gradients near the surface are strongly stabilizing the initial state. Next, a high resolution with $\Delta x = \Delta y = 80 \text{ m}$, $\Delta z = 30 \text{ m}$ is used ($400 \times 400 \times 32$ grid points) using the parameters as in Table 1. The value of the parameter $\text{Ro}^* = (\text{Ra}/(\text{Ta}^{3/2}))^{1/2} = 0.32$, which combined with $\text{Ra} = 10^8$ shows that the simulation is in the 3D turbulent convection regime (Klinger and Marshall 1995). The governing equations were integrated over 0.1 dimensionless units in time corresponding to approximately 12 days.

a. Flow development

This simulation differs from that in Legg et al. (1998) in the initial conditions and parameters, but the flow development obviously shows similar features. Due to the cooling at the surface, a thermal boundary layer forms, which very soon becomes unstable to direct buoyancy driven instabilities. The depth of penetrative convective activity is directly related to the initial stratification. Away from the eddy the convective layer remains limited to the upper 100 m, whereas in the center of the eddy, convection reaches to much greater depth.

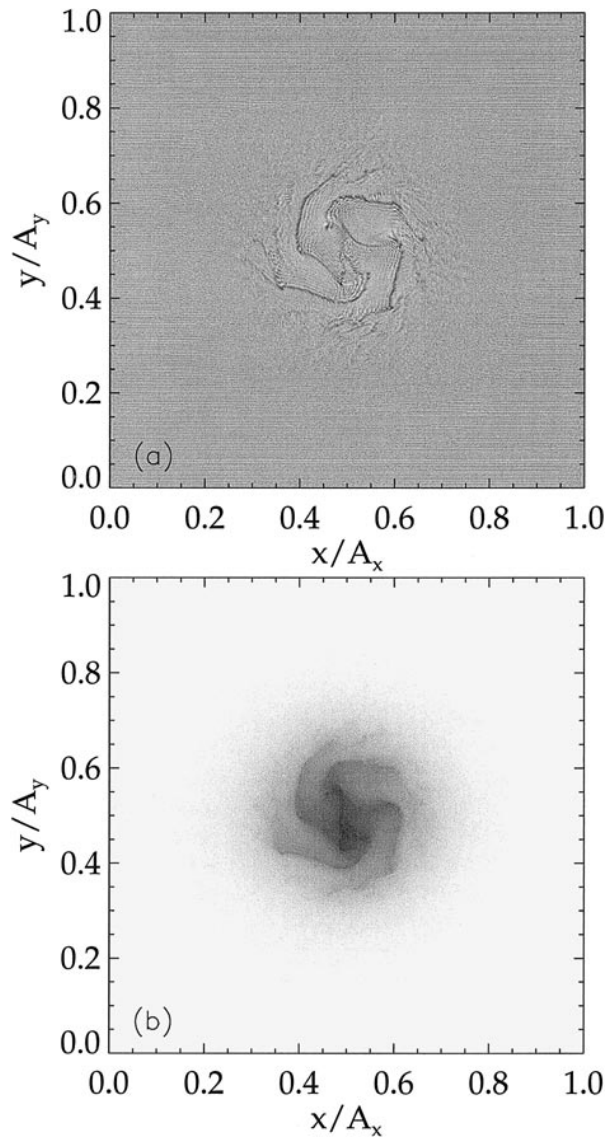


FIG. 7a,b. Horizontal slice at $z = 0.95$ of different fields after three days of cooling. (a) Vertical velocity (dark colors downward, bright colors upward). (b) Temperature (bright colors warm and light, dark colors cold and dense).

After 3 days the convection is active within a radius of about 6 km as can be seen from a slice of the vertical velocity just below the surface ($z = 0.95$) in Fig. 7a. A dominant feature in the vertical velocity field are the spiral structures along which downward velocities have been organized. The width of these spirals is about 100 m and the distance between the arms is a few kilometers. Since the layer is cooled from above, temperature fields (scaled by $HB_0/\kappa g\alpha$) will be shown of the simulations. In the temperature field after 3 days of cooling (Fig. 7b) the small-scale details as in the vertical velocity field can be observed but are superposed on the initial temperature distribution.

In Figs. 7c,d the vertical velocity and temperature

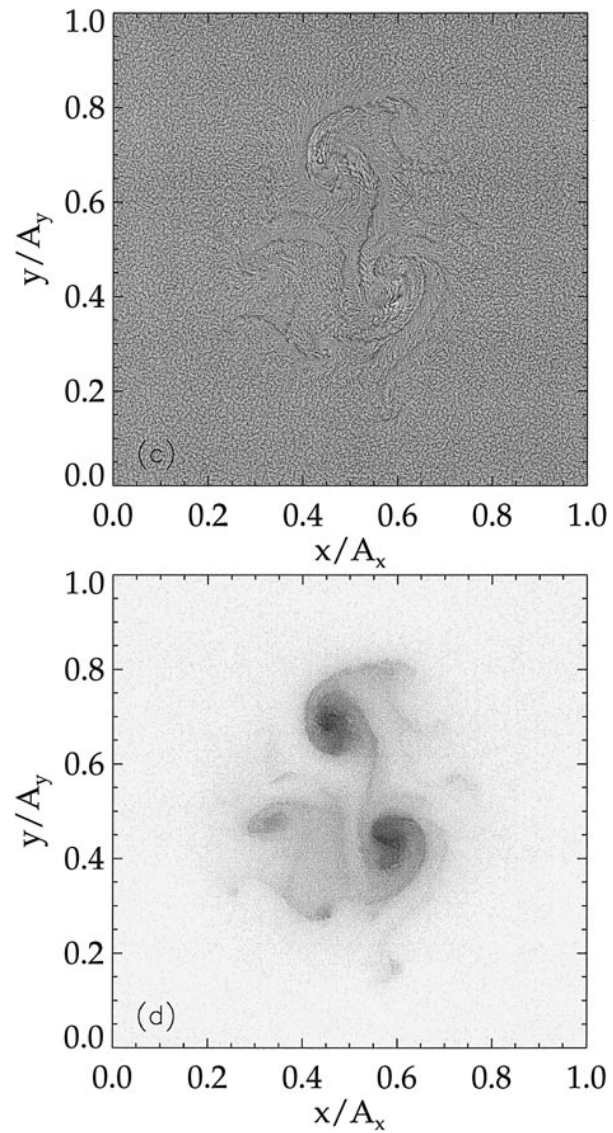


FIG. 7c,d. Horizontal slice at $z = 0.95$ of different fields after six days of cooling. (c) Vertical velocity (dark colors downward, bright colors upward). (d) Temperature (bright colors warm and light, dark colors cold and dense).

fields are shown after 6 days of cooling. The temperature (Fig. 7d) shows two convective patches with a horizontal dimension of about 4 km moving outward of the original convective region. The velocity field shows again many small-scale convective elements (Fig. 7c), but these are organized into larger-scale features that coincide with the cooler patches in the temperature. At a later stage in the evolution both “patches” are found to move outwards from the convective region. The signal of one of these patches passing the point $x/A_x = y/A_y = 0.75$, $z = 0.9$ can be seen in the time series of the azimuthal velocity v (solid) and vertical velocity w (dotted) in Fig. 8 near $t = 120$ h. This figure gives also an impression of the velocity scales during the evolu-

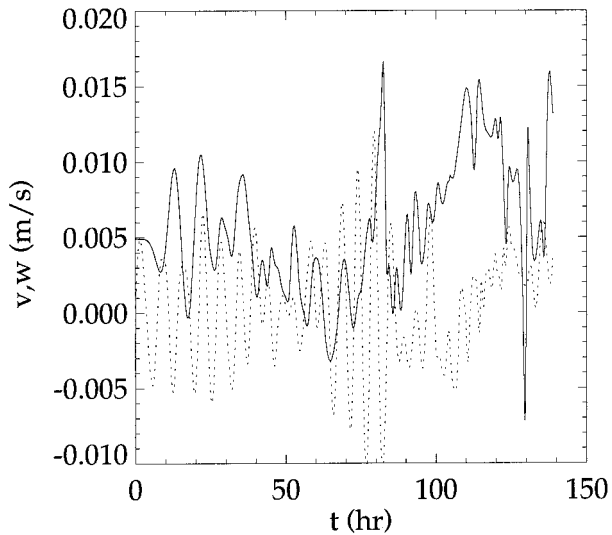


FIG. 8. Time evolution of the azimuthal velocity v (solid) and vertical velocity w (dotted) at the point $x = 0.75A_x$, $y = 0.75A_y$.

tion. The azimuthal velocity v oscillates initially around a mean value of $5 \times 10^{-3} \text{ m s}^{-1}$, which corresponds to the velocity field of the prescribed eddy, up to about 3 days. The timescale of these oscillations corresponds to convective plumes with a size of several 100 m that are advected by the background velocity field. For $t > 60$ h the velocity becomes more irregular corresponding to the breakup of the original eddy into different convective patches. This breakup can also be seen in the vertical velocity showing large amplitude oscillations (the maxima correspond to 10^{-2} m s^{-1}) around that time, which subsequently become irregular.

In the initial stages of the flow development, the scales of motion correspond to those derived earlier in the numerical simulations where localized cooling over a disk within the flow domain was applied (Jones and Marshall 1993). By calculating Ta based on the depth of the unstable thermal boundary layer, using a depth of $\delta = 0.1H$, we find a value of $Ta \approx 200$. This value is sufficiently small to neglect the effect of rotation during the initial stage of convection. This can also be seen from the corresponding timescale of the convective motions in that layer (Deardorff 1980); $t \sim (\delta^2/B_0)^{1/3}$ or $t \approx 4.6 \times 10^3 \text{ s}$, which means that $t < f^{-1}$ and rotation is not (yet) important. The resulting scales for (nonrotating) convection are $l_{\text{conv}} = \delta \approx 100 \text{ m}$, $u_{\text{conv}} = (l_{\text{conv}}B_0)^{1/3} \approx 10^{-2} \text{ m s}^{-1}$. At $t = f^{-1}$, rotational effects become important and the scales $l_{\text{rot}} \sim (B_0/f^3)^{1/2}$, $u_{\text{rot}} \sim (B_0/f)^{1/2}$ are expected (Maxworthy and Narimousa 1994; Fernando et al. 1991; Jones and Marshall 1993). In the present simulation, $l_{\text{rot}} \approx 150 \text{ m}$ and $u_{\text{rot}} \approx 2 \times 10^{-2} \text{ m s}^{-1}$ and, because the difference between rotationally and nonrotationally dominated scales is small, a transition between both regimes cannot be clearly distinguished in Fig. 8.

In agreement with the results of the linear stability

calculation in the previous section the $m = 4$ mode is clearly dominating the results of the numerical simulation, where it can be identified by the four spirals in the vertical velocity (e.g., Fig. 7a). As argued in the previous section, the exact value of the cooling time to calculate the basic states is not important as long as it is small. Apparently, the effect of the convection on the baroclinic instability has been modeled well by the parameterization of the convection through the parameter τ ; that is, only the erosion of the surface stratification is important. The reason may be that the large-scale dynamical effects of the small-scale velocities that result from convection are small.

In the localized cooling case the density anomaly caused by convection, say measured by a reduced gravity g'_c , induces a horizontal density gradient and subsequently a rim current that is susceptible to baroclinic instabilities. However, in our case, a horizontal dynamical density gradient is already present through the geostrophic eddy. The g'_c due to the eddy can be directly obtained from the initial conditions $g'_c = g\Delta\rho$, where $\Delta\rho$ can be estimated by the initial difference between the density in the center of the eddy and that of the background density field. An estimate of g'_c is not so easy to define in our case. Since the cooling is not localized over the eddy, previously used estimates that consider a balance between localized cooling and horizontal transport by the convective patches (Visbeck et al. 1996) are not valid here. Any additional density difference to g'_c will only be due to horizontal mixing since the cooling is homogeneous over the whole surface. The effect of horizontal mixing will be small, at least up to the time where the large-scale perturbations are not yet fully developed. However, an upper bound is certainly given by the estimate based on the near steady state thermal balance from Visbeck et al. (1996), $g'_c = N(B_0R_0)^{1/3}$. If we base g'_c on the surface values, then the ratio g'_c/g'_e for $\tau = 0$ is given by

$$\frac{g'_c}{g'_e} = \frac{N(B_0R_0)^{1/3}\kappa}{A_eHB_0}, \quad (15)$$

and its value will determine whether convection will influence the mean circulation of the eddy or not. In the present simulation, $g'_c/g'_e \approx 3 \times 10^{-4}$ and consequently the rim current induced by convection is negligible compared to the velocity field of the original eddy. This shows that the dominating unstable modes are determined by the initial geostrophic eddy and not by the strength of the surface buoyancy flux.

b. Spectral analysis of the flow patterns

As can be observed in the high-resolution nonhydrostatic simulation there is much energy both in the large scales (baroclinic instability) and the small scales (convection). To look at the energy-containing scales in more detail, two-dimensional discrete Fourier spectra were calculated for the spatial pattern of quantities in

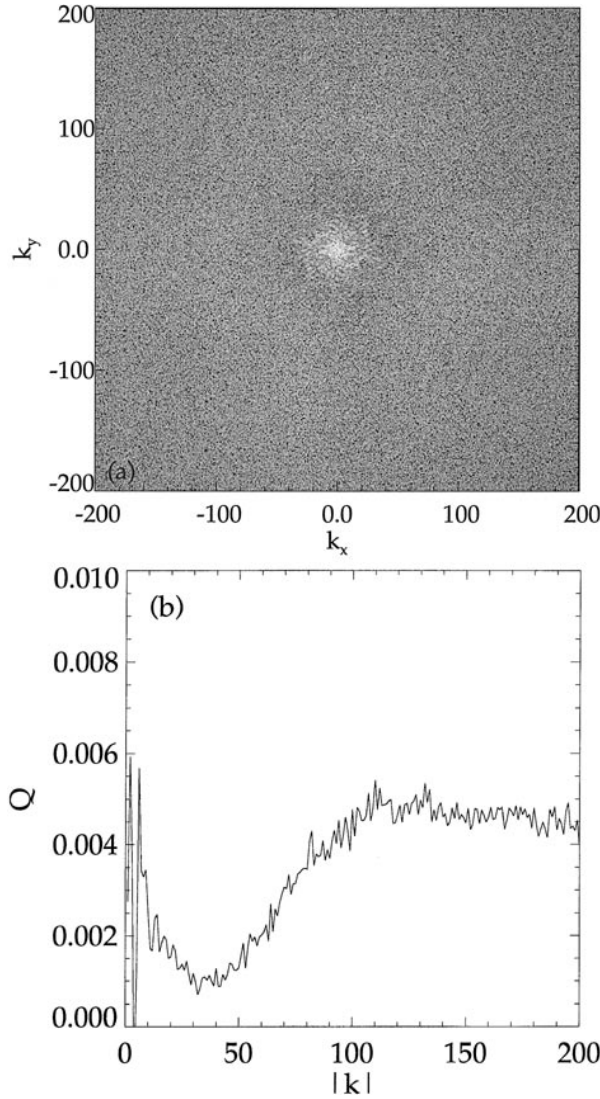


FIG. 9. Analysis of the spatial patterns in the high-resolution simulation at $t^* = 6$ days and a horizontal slice at $z = 0.95$. (a) Grayscale plot of the two-dimensional cospectrum of the vertical velocity and the temperature \hat{Q} as a function of k_x ($-N/2 < k_x < N/2$) and k_y ($-M/2 < k_y < M/2$). Light (dark) colors indicate large (small) values. (b) \hat{Q} as a function of the absolute wave number $|k|$ as obtained from the two-dimensional cospectrum.

a horizontal plane just below the surface. More specific, for any quantity F the (complex) discrete Fourier transform \hat{F} is defined as

$$\hat{F}_{k_x, k_y} = \frac{1}{\sqrt{NM}} \sum_{n=1}^N \sum_{m=1}^M F_{n,m} \exp \left[-i2\pi \left(\frac{nk_x}{N} + \frac{mk_y}{M} \right) \right], \quad (16)$$

where

$$k_x = -N/2, \dots, -1, 0, 1, \dots, N/2,$$

$$k_y = -M/2, \dots, -1, 0, 1, \dots, M/2$$

and the $F_{n,m}$ are the values of F at the grid points. An important quantity to consider in the problem is the

TABLE 2. Spectral distribution of the vertical heat flux for the different simulations considered. The entry $(wT)_b$ is the “baroclinic” component, defined as the contribution to the total heat flux wT for $k < 40$. The quantity $(wT)_c$ is the “convective” component, defined as the contribution to wT for $k > 40$ and $(wT)_b + (wT)_c = wT$. IM and CA are different types of convective adjustment as explained in the text.

$n \times m$	Type of adjustment	wT	$(wT)_b$	$(wT)_c$
400×400	nonhydrostatic	0.796	0.073	0.723
256×256	IM, $\eta = 0$	0.174	0.121	0.053
128×128	IM, $\eta = 0$	0.133	0.110	0.024
128×128	CA	0.153	0.132	0.021
256×256	IM, $\eta = 1$	0.071	0.067	0.004
128×128	IM, $\eta = 1$	0.110	0.105	0.005

vertical convective heat flux $Q = wT$. All the presented spectra are therefore chosen to be cospectra of vertical velocity w and temperature T . The cospectrum \hat{Q} is defined as

$$\hat{Q} = \text{Re}(\hat{w})\text{Re}(\hat{T}) + \text{Im}(\hat{w})\text{Im}(\hat{T}), \quad (17)$$

with Re and Im indicating real and imaginary part and \hat{w} and \hat{T} defined as in (16). It follows that \hat{Q} is real and the sum over the (discrete) wavenumbers of the cospectrum \hat{Q} equals the integrated vertical heat flux Q (Stull 1988).

At $t^* = 6$ days, a gray shade plot of \hat{Q}_{k_x, k_y} is shown in Fig. 9a for a slice at $z = 0.95$, which corresponds to the pattern in Figs. 7c,d. The bright area enclosing the center shows the energy containing large scales. Much energy is still contained in the initial eddy, corresponding to $k_x = k_y = 0$, other large scales arise through its baroclinic development. Enclosing this center area is a band of relatively small amplitude followed by a broad small-scale band corresponding to the convective scales of $O(10^2 \text{ m})$. The corresponding spatial scale of a specific wavenumber can be found from $\lambda = L/|k|$, $|k| = (k_x^2 + k_y^2)^{1/2}$, where $L = 32 \text{ km}$ is the horizontal length of the domain.

The dominant spatial scales can be seen more easily in a plot of \hat{Q} as a function of $|k|$ (Fig. 9b). Two bands of high energy containing scales are again seen, which can be roughly divided into a large-scale band $0 < |k| < 40$ and a small-scale band $40 < |k| < 200$. The two spectral bands in Fig. 9b motivate one to compute a band averaged spectral amplitude of the convective heat flux. These values are given as $(wT)_b$, for the large scales ($k < 40$) and $(wT)_c$ for the small scales ($k > 40$) in the first row of Table 2 for the nonhydrostatic high-resolution simulation. Most of the energy (about 90%) is contained in the small scales. We will use these band averages in the subsequent section to study the issue of representation of convection in hydrostatic models.

5. Convection in hydrostatic models

Having established the basic characteristics of the flow development as observed in the high resolution

nonhydrostatic simulation, we now investigate how these are represented in hydrostatic models. A hydrostatic version of the code can be easily developed from the nonhydrostatic code and, since the approach differs from that in Marshall et al. (1997a), more details are presented in the appendix.

a. Convective adjustment

In the nonhydrostatic model, convection is explicitly resolved and no adaptations are needed when the stratification becomes locally (statically) unstable. In hydrostatic models, the effects of convection have to be parameterized and several ad hoc procedures, generally referred to as convective adjustment, are used. In all these procedures, the temperature (and salinity) fields are locally adjusted in such a way that a stable stratification is achieved. In the first procedure, which we will indicate by classical adjustment (CA), the temperature is explicitly mixed in adjacent vertical levels of the water column if the density stratification is unstable. This procedure has to be repeated a number of times at each time step in the evolution of the flow, as an iteration toward complete removal of static instabilities (Cox 1984). A variation of this technique is suggested by Marotzke (1991) and others (Yin and Sarachik 1994; Rahmstorf 1995) in which groups of levels in the water column are treated as one convective region. The latter procedure was implemented since it is guaranteed that the liquid is stably stratified after the procedure terminates. This occurs within one time step of the model, and hence it is assumed that the timescale of convective mixing is much smaller than the time step of the numerical model. Furthermore, it is assumed that the convection only mixes quantities vertically; no horizontal mixing is involved.

The other procedure of convective adjustment is indicated by implicit mixing (IM) and assumes that the effect of convection on a subgrid scale can be modeled by a large vertical diffusion coefficient for the tracers (Cox 1984). Hence, the vertical mixing is parameterized as

$$\frac{\partial}{\partial z} \left(K_v \frac{\partial T}{\partial z} \right) \quad (18)$$

with the mixing coefficients given by

$$K_v = \kappa + K_v^c, \quad (19)$$

where κ is the background value (as in Table 1) and K_v^c models the subgrid-scale convection as an additional diffusive process. The value of K_v^c is large in areas with unstable stratification and zero otherwise. A value of K_v^c can be estimated from a straightforward mixing length argument using the appropriate velocity U and length scales L for convection. In the rotationally controlled regime, one would have $U = \sqrt{B_0/f}$ and a length

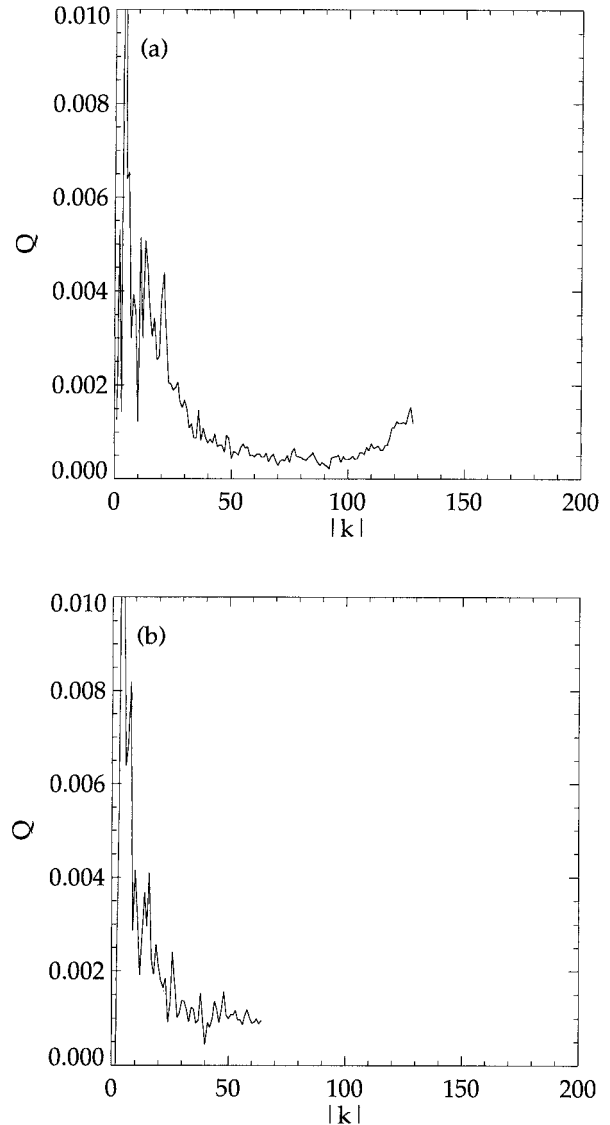


FIG. 10. (a) Two-dimensional cospectrum \hat{Q} obtained from a horizontal slice at $z = 0.95$ for the hydrostatic model after six days of cooling. In these results, $\eta = 0$ and a $256 \times 256 \times 32$ grid is used. (b) As (a) but with a $128 \times 128 \times 32$ grid.

scale $L = \sqrt{B_0/f^3}$. This scaling leads to a mixing coefficient of

$$K_v^c = UL = \frac{B_0}{f^2}, \quad (20)$$

which gives values of $K_v^c = O(10 \text{ m}^2 \text{ s}^{-1})$, a value about 100 times larger than the background diffusivity of $\kappa = 0.1 \text{ m}^2 \text{ s}^{-1}$. For all subsequent calculations where IM is used a value of $K_v^c = 10 \text{ m}^2 \text{ s}^{-1}$ is chosen. Instead of this estimate for the mixing length scale one could also use the depth of the mixed layer as suggested in Klinger et al. (1996) but this does not lead to an order of magnitude difference.

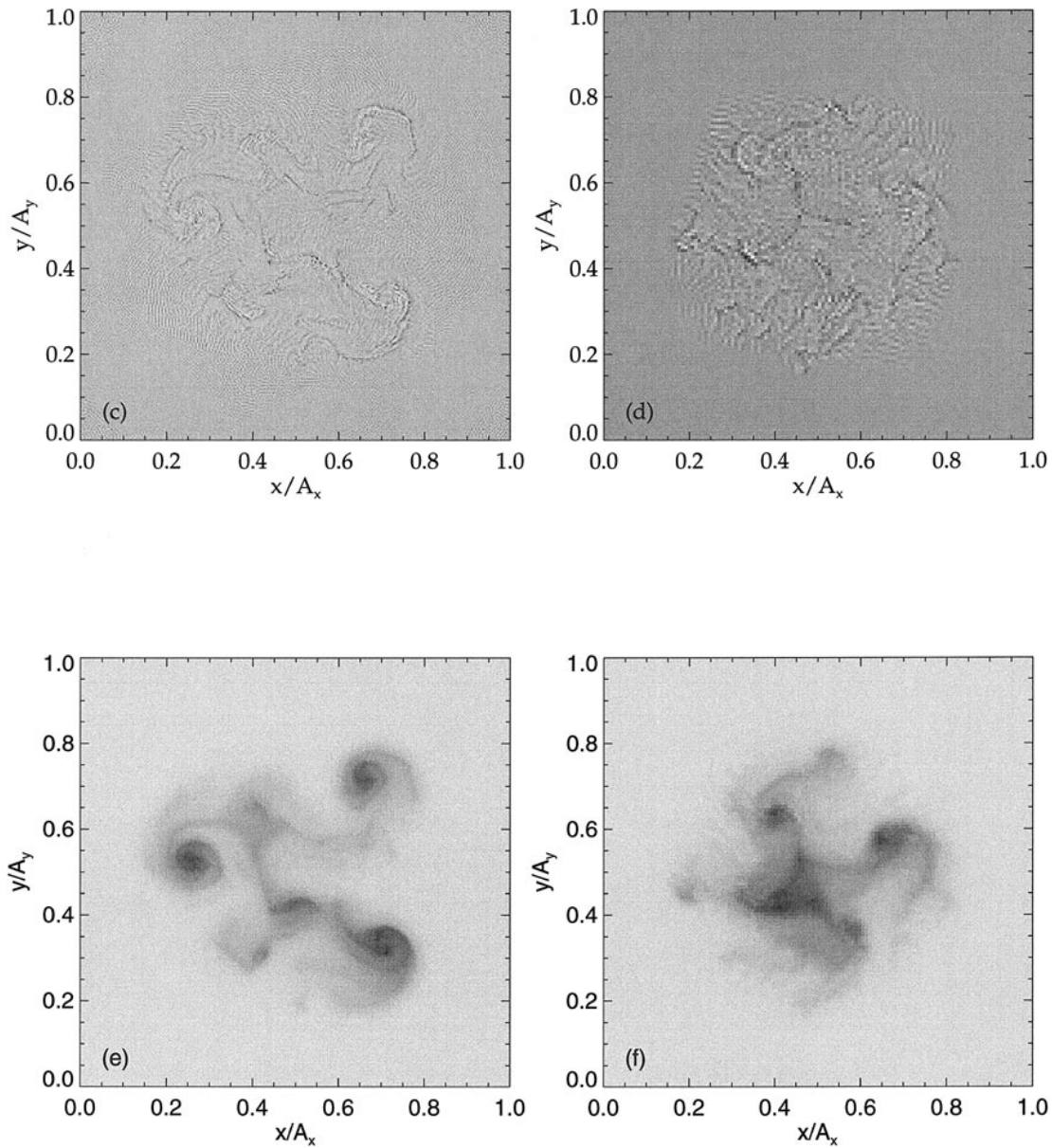


FIG. 10. (Continued) (c) Vertical velocity field corresponding with (a). (d) Vertical velocity field corresponding with (b). (e) Temperature field corresponding with (a). (f) Temperature field corresponding with (b).

b. Results

The total heat flux Q is defined as

$$Q = wT - K_v \frac{\partial T}{\partial z}. \quad (21)$$

In the nonhydrostatic model, the range of scales is large and, in particular, the small scales contribute to the advective term wT , whereas the diffusive term $K_v \partial T / \partial z$ in (21) is relatively small (K_v equals κ). The basic idea of the adjustment schemes in hydrostatic models is that the contribution of the large scales to the heat flux Q should be represented well, whereas the small-scale contribu-

tion to wT is parameterized by the convective adjustment as in (18). In other words, there should be no small-scale amplitude in the explicitly resolved part of wT in hydrostatic models that employ a form of convective adjustment. The contribution of the smaller convection scales must be represented by the relatively large term $K_v^c \partial T / \partial z$.

In Fig. 10a, the cospectrum of \hat{Q} is shown for the IM scheme (18) using a horizontal resolution of 256×256 . In Table 2, the corresponding band amplitudes are given in the second row. Although the contribution of the small scales reduces to 30% of the total, it certainly does not vanish as would be desired. In fact, Fig. 10a

shows erroneous activity in the small scales. The activity increases toward the smallest resolved scales, indicating a source at the grid scale that most likely has a numerical origin. In Fig. 10c, these small-scale features can be observed in the vertical velocity pattern. As a consequence of the presence of these erroneous scales, the breakup of the eddy is quite different from the reference case, as can be seen for the temperature field in Fig. 10e. For a horizontal resolution of 128×128 , the spectrum (Fig. 10b), vertical velocity (Fig. 10d), and band amplitudes (the third row of Table 2) show similar behavior. Here again, erroneous small-scale activity is present, although the total amount is less, due to the fact that the highest wavenumber present at that resolution is only $k = 64$. This is similar to the results for CA (fourth row of Table 2) of which the spatial fields and spectrum are not shown.

The origin of this small-scale activity is most likely the occurrence of nonresolved boundary layers in areas where convection occurs. The essential difficulty can be illustrated by a simple reasoning that only assumes diffusive processes. Consider the timescale of vertical exchange that is associated with the convective adjustment to be t_{mix} . Within this time, horizontal temperature differences are created on the smallest resolved (grid) scales. These horizontal gradients will lead to diffusive boundary layers of which the thickness can be readily estimated from classical diffusion theory (Carslaw and Jeager 1959); that is, $\delta = (\pi t_{\text{mix}} K_h)^{1/2}$, where K_h is the horizontal diffusivity. The boundary layer thickness δ should be resolved by the horizontal grid spacing; otherwise they lead to spurious activity on the smallest scales. An estimate for the condition on the minimal horizontal resolution is

$$\Delta x < (\pi t_{\text{mix}} K_h)^{1/2}. \quad (22)$$

If this boundary layer is not resolved, large numerical errors may result, which can completely destroy the accuracy of the solution and have other undesirable, nonphysical effects. Another possible cause for the small-scale activity is hydrostatic overturning, as discussed in Marshall et al. (1997b). Hydrostatic models are not stable in the presence of statically unstable gradients but exhibit a type of convection. However, since in convective conditions the hydrostatic assumption is not valid, it is not clear what value can be attributed to this “hydrostatic convection.”

If a large vertical diffusivity is used in the convective adjustment procedure (IM), the timescale of vertical exchange and consequently the timescale in which the horizontal boundary layers are formed can be found using the “convective mixing” coefficient K_v^c . The vertical exchange timescale is now given by $\Delta t = D^2/K_v^c$, where D is a vertical scale over which mixing takes place. Consequently, Eq. (22) can be written as a condition for the horizontal diffusivity

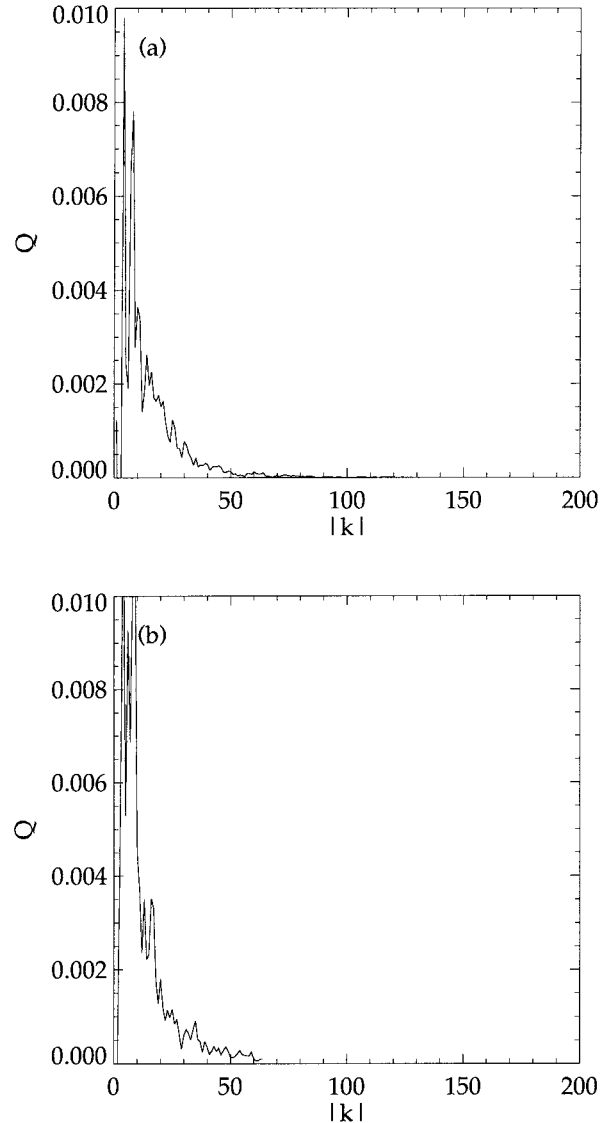


FIG. 11. (a) Two-dimensional cospectrum \hat{Q} obtained from a horizontal slice at $z = 0.95$ for the hydrostatic model after 6 days of cooling. In these results, $\eta = 1$ and a $256 \times 256 \times 32$ grid is used. (b) As (a) but with a $128 \times 128 \times 32$ grid.

$$K_h^c > \frac{\Delta x^2 K_v^c}{\pi D^2}. \quad (23)$$

On the other hand, if an algorithm is used that completely removes unstable vertical gradients within one time step (i.e., CA), the timescale on which the horizontal boundary layers are created is equal to the time step of the numerical scheme Δt . Equation (22) can now be written as a condition for the time step

$$\Delta t > \frac{\Delta x^2}{\pi K_h}. \quad (24)$$

From (24) it follows immediately that numerical problems are expected if the time step Δt is decreased, which

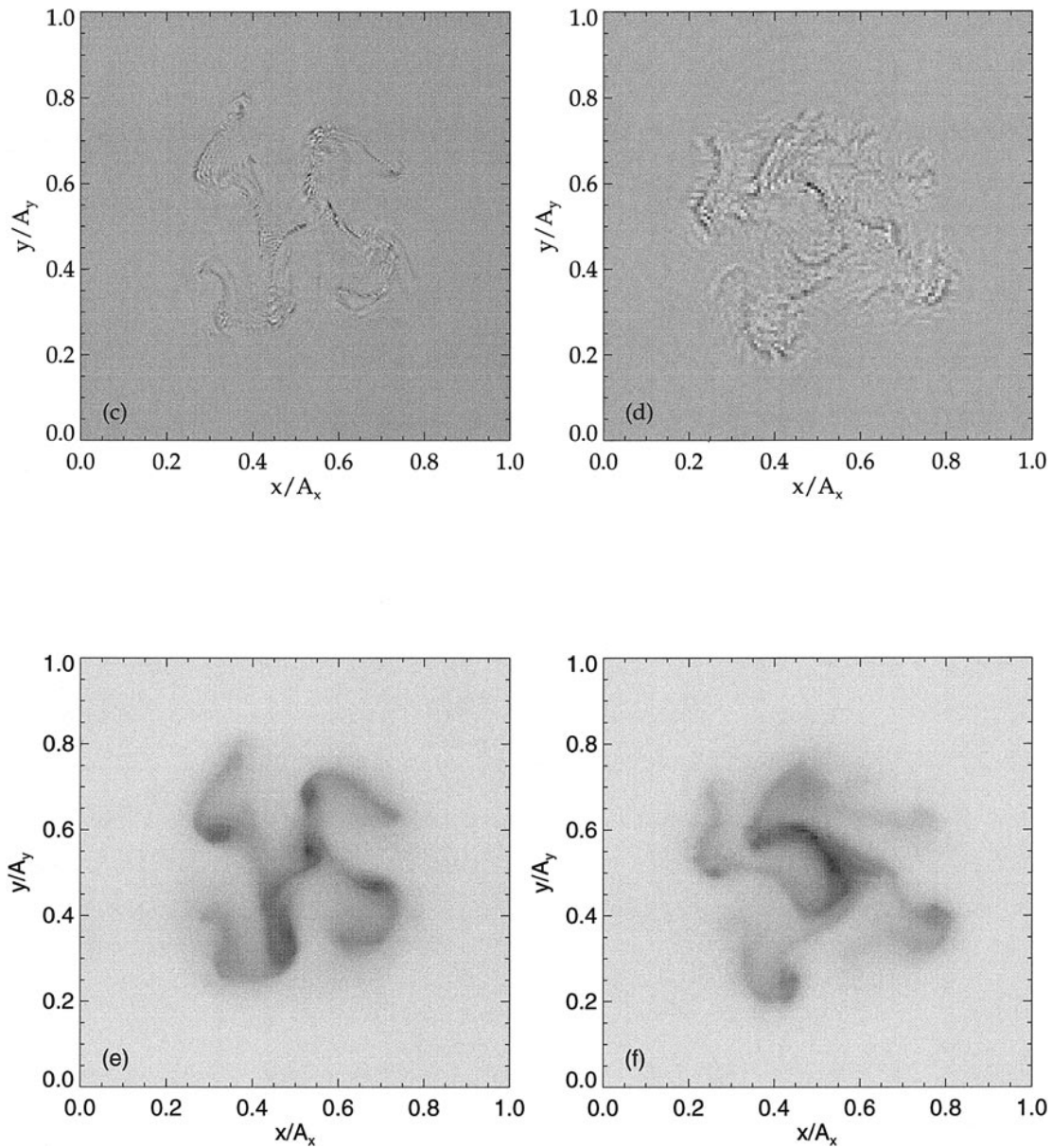


FIG. 11. (Continued) (c) Vertical velocity field corresponding with (a). (d) Vertical velocity field corresponding with (b). (e) Temperature field corresponding with (a). (f) Temperature field corresponding with (b).

is [similar to the grid-scale instability in Cessi (1996)] a very undesirable quality in any numerical integration.

c. Modified adjustment scheme

To test whether this simple picture is indeed responsible for the small-scale activity, as seen in the two-dimensional spectra for the hydrostatic model, several simulations were performed in which additional horizontal diffusion was added locally in areas where convective adjustment occurred. The IM procedure was

used; in this case, the Laplacian diffusion terms are written as

$$\nabla_h \cdot (K_h \nabla_h \rho) + \frac{\partial}{\partial z} \left(K_v \frac{\partial \rho}{\partial z} \right) \quad (25)$$

with $\nabla_h = (\partial/\partial x, \partial/\partial y)$. The mixing coefficients are given by

$$K_h = \kappa + K_h^c; \quad K_v = \kappa + K_v^c, \quad (26)$$

where the superscript *c* again refers to values due to convective adjustment.

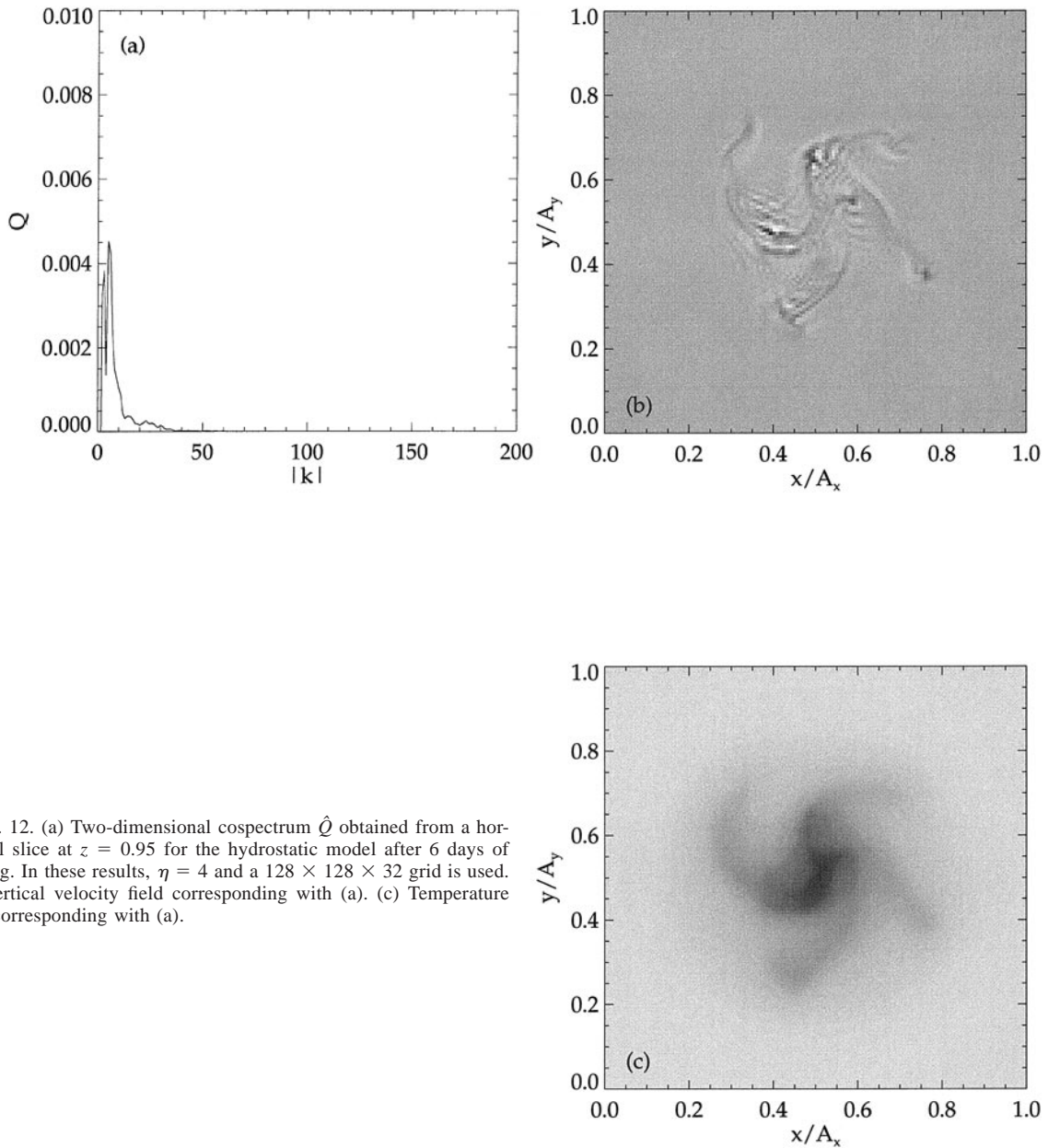


FIG. 12. (a) Two-dimensional cospectrum \hat{Q} obtained from a horizontal slice at $z = 0.95$ for the hydrostatic model after 6 days of cooling. In these results, $\eta = 4$ and a $128 \times 128 \times 32$ grid is used. (b) Vertical velocity field corresponding with (a). (c) Temperature field corresponding with (a).

In the simulations we take $K_h^c = \eta K_v^c$ with $K_v^c = 10 \text{ m}^2 \text{ s}^{-1}$ and $\eta = 1$. This is believed to be physically realistic in a high-resolution hydrostatic model and also guarantees the absence of spurious numerical behavior, as described above, if the value of η is such that Eq. (23) is satisfied. For the coarsest resolution ($\Delta x = 240 \text{ m}$) indeed (23) is satisfied with $\eta = 1$. From a physical point of view, the choice $\eta = 1$ also makes sense since, for three-dimensional convection, horizontal and vertical scales of convective elements that have to be parameterized are the same. Consequently horizontal and vertical mixing that result from this convective activity should also be the same.

In Figs. 11a,b, the cospectra \hat{Q} are shown for equal vertical and horizontal diffusivities ($\eta = 1$) for both $256 \times 256 \times 32$ and $128 \times 128 \times 32$ resolution. In both cases the small-scale activity has decreased significantly, in correspondence with the patterns that are shown in Figs. 11c–f. From Table 2, which shows the band amplitudes in this case, it may be observed that the convective heat flux induced by the “baroclinic scales” ($k < 40$) has roughly the same amplitude as the corresponding heat flux in the reference run with the non-hydrostatic model. With $\eta = 4$ and a resolution of $128 \times 128 \times 32$ the small-scale energy is decreased enormously (Fig. 12a), but the breakup of the eddy is now

diffusively controlled. Although an $m = 4$ mode is still present, the horizontal diffusivity is now too large, the amplitude of the baroclinic disturbance remains small, and the eddy is not breaking up into convective patches, which move out of the original convective region (Figs. 12b,c). Hence, a too large value of K_h modifies the large-scale flow development too much.

6. Summary and discussion

In this paper, focus was on the localization process of convection by means of the cooling of a geostrophic eddy. Instead of a localized buoyancy source into a liquid without horizontal density gradients, a homogeneous buoyancy source was considered into a liquid with a dynamically preconditioned density field caused by the presence of a geostrophic eddy. Rather than making a detailed analysis of the flow from numerical simulations as in Legg et al. (1998), the linear stability analysis of geostrophic eddies was carried out.

The first result is that convection strongly influences the large-scale instability of the geostrophic eddy, mainly through its erosion of the stable surface stratification. Initially, the eddy is stable because of large vertical density gradients near the surface. However, these gradients are not sufficient to prevent convection. The immediate effect of surface cooling and the developing convection is the erosion of the vertical density gradients. This effect was parameterized by the cooling parameter τ , which ranged from no cooling ($\tau = 0$) to a situation modified by convection as a result of surface cooling ($\tau = 1$). The linear stability analysis shows that the increase of τ favors the large-scale instability of the eddy.

Over the range of eddy sizes investigated, it appears that the wavelength is independent of the eddy scale. Small eddies lead to smaller values of the azimuthal wavenumber, but such that the product of eddy size and azimuthal wavenumber remains constant. There is no a priori reason why this wavelength should be four times the appropriate internal Rossby deformation radius L_ρ , like in the Eady problem. However, when this is assumed, a value $L_\rho = 1.4$ km is obtained. Although for the situation at $\tau = 0$, the values of L_ρ at the surface range from 7–17 km, the effect of τ is to decrease L_ρ significantly and effectively it is zero locally near the surface for $\tau = 1$. It is interesting that the ratio of eddy radius $H/\sqrt{2\alpha_e}$, and L_ρ is in this case larger than 2 for all the eddies. This indicates, assuming the necessary condition for instability (Pedlosky 1985) applies here, that one needs indeed such a small L_ρ for the eddy to become unstable.

For the standard eddy, the $m = 4$ mode was found to be most unstable. The corresponding flow pattern was found in the high-resolution simulation as the dominant large-scale response. The horizontal density gradients induced by convection are, for the case considered, much smaller than those present due to the geostrophic

eddy. The large-scale flow development is therefore not influenced much by this additional horizontal gradient and therefore the $m = 4$ flow pattern is dominating the response over a long time interval. Further evolution of the flow is complicated since the developing baroclinic instabilities modify the density field and affect the convective activity. Pairs of convective patches are formed that split off from the original convective area and migrate in opposite directions.

The differences between this flow development and that of the localized cooling case were extensively discussed in Legg et al. (1998). With localized cooling, geostrophic adjustment of the well-mixed column of water leads to a rim current. The baroclinic instability of this current leads to breakup of column and flow outside the region of cooling. Although the latter flow modifies the density field, it does not lead to significant convection because it is not cooled at the surface. With a prescribed eddy, the situation is quite different. As the eddy becomes baroclinically unstable, the density outside the eddy gets modified. This may lead again to convection, even in regions far from the initial location of convection. Hence, there is a more intricate coupling between the large-scale flow development and the small-scale convection. The net effect is that due to lateral mixing, the density difference between the eddy and the background field *decreases* as opposed to the numerical simulation of Jones and Marshall (1993) where the density difference *increases* due to the localized cooling at the surface.

To look at the effect of representation of convection in hydrostatic models on the large scale flow development, two-dimensional cospectra of convective heat flux for the high resolution nonhydrostatic simulation were compared to several simulations, at different resolution, in hydrostatic models. Erroneous small-scale energy was shown to be present in the hydrostatic models using either type of convective adjustment. The origin of this small-scale energy is numerical and present due to inadequate representation of the horizontal gradients, which arise on the grid scale due to convective adjustment. A constraint, involving the horizontal mixing of the particular scalar, the horizontal resolution, and the characteristic vertical mixing timescale, was derived to avoid this spurious behavior. These errors are not expected to disappear when more sophisticated vertical adjustment is used, such as the slow convective adjustment scheme proposed by Klinger et al. (1996). For the eddy flow evolution, it was demonstrated that erroneous high energy small-scales disappear once this constraint is satisfied by adding horizontal diffusion in areas where convection occurs.

It was demonstrated that classical convective adjustment at too coarse resolution is inadequate to simulate the correct large-scale flow development. This may have implications for the simulation of some phenomena in OGCMs. For example, it has been suggested that rapid climate transitions may occur (through transitions between stable equilibria) due to different positions at

which convection occurs (Rahmstorf 1995; Lenderink and Haarsma 1994). It appears that these transitions occur at the grid scale with different equilibria associated with convection on or off at the particular point. Some recent fundamental studies have also indicated problems with convective adjustment in hydrostatic models. In Vellinga (1998), a study is presented that shows the existence of multiple equilibria within a zonally averaged model of the thermohaline overturning circulation that are most likely a side effect of convective adjustment. Cessi (1996) describes a grid scale oscillatory instability due to the CA procedure within a very simple model that is always present if the adjustment is instantaneous. The problems we have addressed here are of similar nature: that CA removes unstable vertical density gradients instantaneously may create *horizontal* density gradients on a scale that is equal to the grid size. The grid size, time step, and horizontal diffusion of the models used both in Rahmstorf (1995) and Lenderink and Haarsma (1994) certainly do not satisfy the criterion (24), and trouble can be expected. The issue of spurious numerical results due to convective adjustment adds to an increasing amount of evidence that one has to be very careful to put physical significance to results that depend crucially on such an algorithm.

Acknowledgments. We gratefully acknowledge the support of Cray Research, the Netherlands (Drs. M. Cutts and R. van Pelt) for their assistance to run the numerical code on a parallel machine and for providing dedicated computing time on the Cray-C90/16 in Minneapolis, Minnesota.

APPENDIX

Numerical Methods

The governing nonhydrostatic equations are discretized in space using second-order central differences on an equidistant staggered grid. Together with the boundary conditions, the discretized momentum equations form a closed set of (coupled) ordinary differential equations, which can be written as

$$\frac{\partial \mathbf{u}_{i,j,k}}{\partial t} = -\nabla p_{i,j,k} + \mathbf{F}_{i,j,k}(\mathbf{u}, \rho), \quad (\text{A1})$$

for $i = 1, \dots, N$; $j = 1, \dots, M$; $k = 1, \dots, L$. Here the $\mathbf{F}_{i,j,k}$ represent the (discretized) advective, diffusive and buoyancy terms. The set of equations (A1) is integrated in time using an Adams–Bashforth method that is second-order accurate in time; that is,

$$\mathbf{u}_{i,j,k}^{n+1} = \mathbf{u}_{i,j,k}^n + \Delta t \left(\frac{3}{2} (\mathbf{F}_{i,j,k}^n - \nabla p_{i,j,k}^n) - \frac{1}{2} (\mathbf{F}_{i,j,k}^{n-1} - \nabla p_{i,j,k}^{n-1}) \right), \quad (\text{A2})$$

where n indicates the time index. Taking the divergence of (A2) gives

$$D_{i,j,k}^{n+1} = D_{i,j,k}^n + \Delta t \left(\frac{3}{2} (R_{i,j,k}^n - \nabla^2 p_{i,j,k}^n) - \frac{1}{2} (R_{i,j,k}^{n-1} - \nabla^2 p_{i,j,k}^{n-1}) \right), \quad (\text{A3})$$

where $D = \nabla \cdot \mathbf{u}$ and $R = \nabla \cdot \mathbf{F}$. The pressure acts in this case as a constraint which ensures that the flow will remain divergence-free. To solve for the pressure at every time step, (A3) is rearranged and we demand $D_{i,j,k}^{n+1} = 0$. This leads to

$$\nabla^2 p_{i,j,k}^n = \frac{2}{3} D_{i,j,k}^n + \Delta t \left(R_{i,j,k}^n - \frac{1}{3} (R_{i,j,k}^{n-1} - \nabla^2 p_{i,j,k}^{n-1}) \right). \quad (\text{A4})$$

At time n , all the terms of the right-hand side of (A4) are known, so we can solve for $p_{i,j,k}^n$. Boundary conditions for the pressure at the upper and lower boundary are found using (2a) and realizing that $w = 0$ at $z = 0$ and $z = 1$. Hence,

$$z = 0, 1: \quad \frac{\partial p}{\partial z} = \frac{\partial^2 w}{\partial z^2} + \text{Ra} \rho = -\frac{\partial}{\partial x} \frac{\partial u}{\partial z} - \frac{\partial}{\partial y} \frac{\partial v}{\partial z} + \text{Ra} \rho. \quad (\text{A5})$$

From (A5), it is found that if and only if body forces vanish and stress-free conditions are prescribed at the boundaries, the boundary conditions for the pressure at both boundaries reduce to $\mathbf{n} \cdot \nabla p = 0$, which are the boundary conditions that are normally used in similar numerical models.

The nonhydrostatic model can be changed into a hydrostatic model using a small amount of changes. The result is a fast and efficient algorithm to compute transient behavior of three-dimensional hydrostatic flows in simple geometries. The hydrostatic assumption implies that the dynamical vertical accelerations are neglected. This changes the nondimensional momentum equations (2a) into

$$\frac{\partial u}{\partial t} + \mathbf{u} \cdot \nabla u - \sqrt{\text{Ta}} v = -\frac{\partial p}{\partial x} + \nabla^2 u \quad (\text{A6a})$$

$$\frac{\partial v}{\partial t} + \mathbf{u} \cdot \nabla v + \sqrt{\text{Ta}} u = -\frac{\partial p}{\partial y} + \nabla^2 v \quad (\text{A6b})$$

$$0 = -\frac{\partial p}{\partial z} - \text{Ra} \rho. \quad (\text{A6c})$$

The continuity equation (2b), the conservation equation for the density (2c), and the appropriate boundary conditions complete the model. We can write (A6a,b) as

$$\frac{\partial u}{\partial t} = -\frac{\partial p}{\partial x} + F_u \quad (\text{A7a})$$

$$\frac{\partial v}{\partial t} = -\frac{\partial p}{\partial y} + F_v, \quad (\text{A7b})$$

where again F_u , F_v represent the diffusive, advective and body force terms.

In the hydrostatic formulation, the pressure cannot be used as a constraint to ensure the absence of divergence because we are using (2b) to calculate the vertical velocity w . However if we integrate (2b) from $z = 0$ to $z = 1$, we find (with $w = 0$ on $z = 0$ and $z = 1$)

$$\frac{\partial \bar{u}}{\partial x} + \frac{\partial \bar{v}}{\partial y} = 0, \quad (\text{A8})$$

where an overbar indicates the vertically averaged quantities. Integrating equations (A7) vertically gives

$$\frac{\partial \bar{u}}{\partial t} = -\frac{\partial \bar{p}}{\partial x} + \bar{F}_u \quad (\text{A9a})$$

$$\frac{\partial \bar{v}}{\partial t} = -\frac{\partial \bar{p}}{\partial y} + \bar{F}_v. \quad (\text{A9b})$$

Taking the divergence of equations (A9) leads to

$$\frac{\partial \bar{D}}{\partial t} = -\nabla_h^2 \bar{p} + \bar{R}, \quad (\text{A10})$$

with $\bar{D} = \partial \bar{u}/\partial x + \partial \bar{v}/\partial y$ and $\bar{R} = \partial \bar{F}_u/\partial x + \partial \bar{F}_v/\partial y$.

Using the Adams–Bashforth time stepping scheme, a two-dimensional Poisson equation for \bar{p} is obtained after rearranging (A10); that is,

$$\nabla_h^2 \bar{p}_{i,j}^n = \frac{2}{3} \bar{D}_{i,j}^n + \Delta t \left(\bar{R}_{i,j}^n - \frac{1}{3} (\bar{R}_{i,j}^{n-1} - \nabla^2 \bar{p}_{i,j}^{n-1}) \right). \quad (\text{A11})$$

Using (A6c), the total pressure field is

$$p = \text{Ra} \int_1^z \rho dz' + p_0, \quad (\text{A12})$$

where $p_0(x, y)$ is the surface pressure. Using \bar{p} as obtained from (A11), p_0 is easily calculated from

$$\bar{p} = \int_0^1 p dz = \text{Ra} \int_0^1 \int_1^z \rho dz' dz + p_0, \quad (\text{A13})$$

and hence the pressure field is completely determined.

REFERENCES

- Alverson, K., and W. B. Owens, 1996: Topographic preconditioning of open-ocean deep convection. *J. Phys. Oceanogr.*, **26**, 2196–2213.
- Carlsaw, H. S., and J. C. Jeager, 1959: *Conduction of Heat in Solids*. Oxford University Press, 510 pp.
- Cessi, P., 1996: Grid-scale instability of convective-adjustment schemes. *J. Mar. Res.*, **54**, 407–420.
- Chapman, D., and G. Gawarkiewicz, 1997: Shallow convection and buoyancy equilibration in an idealized coastal polynya. *J. Phys. Oceanogr.*, **27**, 555–566.
- Coates, M. J., and G. N. Ivey, 1997: On convective turbulence and the influence of rotation. *Dyn. Atmos. Oceans*, **25**, 217–232.
- , —, and J. R. Taylor, 1995: Unsteady, turbulent convection into a rotating linearly stratified fluid: Modeling deep ocean convection. *J. Phys. Oceanogr.*, **25**, 3032–3050.
- Cox, M., 1984: A primitive equation, three-dimensional model of the ocean. Tech. Rep. 1, GFDL Ocean Group, 75 pp. [Available from Geophysical Fluid Dynamics Laboratory, P.O. Box 308, Princeton, NJ 08542-0308.]
- Dearhoff, J. F., 1980: Stratocumulus-capped mixed-layers derived from a three dimensional model. *Bound.-Layer Meteor.*, **18**, 495–527.
- Eady, E. T., 1949: Long waves and cyclone waves. *Tellus*, **1**, 33–52.
- Fernando, H. J. S., R. Chen, and D. L. Boyer, 1991: Effects of rotation on convective turbulence. *J. Fluid Mech.*, **228**, 513–547.
- Gascard, J. C., and R. A. Clarke, 1983: The formation of Labrador sea water. Part II: Mesoscale and smaller-scale processes. *J. Phys. Oceanogr.*, **13**, 1779–1797.
- Gawarkiewicz, G., and D. Chapman, 1995: A numerical study of dense water formation and transport on a shallow, sloping continental shelf. *J. Geophys. Res.*, **100**, 4489–4507.
- Griffiths, R. W., and P. F. Linden, 1981: The stability of vortices in a rotating, stratified fluid. *J. Fluid Mech.*, **105**, 283–316.
- Hide, R., and P. Mason, 1975: Sloping convection in a rotating fluid. *Adv. Phys.*, **24**, 45–100.
- Johannessen, O. M., S. Sandven, and J. A. Johannessen, 1991: Eddy-related winter convection in the boreas basin. *Deep Convection and Deep Water Formation in the Oceans*, P. C. Chu and J. C. Gascard, Eds., Elsevier Science, 87–105.
- Jones, H. J., and J. Marshall, 1993: Convection with rotation in a neutral ocean: A study of open ocean deep convection. *J. Phys. Oceanogr.*, **23**, 1009–1039.
- Killworth, P. D., 1983: Deep convection in the world ocean. *Rev. Geophys. Space Phys.*, **21**, 1–26.
- Klinger, B. A., and J. Marshall, 1995: Regimes and scaling laws for rotating deep convection in the ocean. *Dyn. Atmos. Oceans*, **21**, 227–256.
- , —, and U. Send, 1996: Representation of convective plumes by vertical adjustment. *J. Geophys. Res.*, **101**, 18 175–18 182.
- Legg, S., J. McWilliams, and J. Gao, 1998: Localization of deep convection by a mesoscale eddy. *J. Phys. Oceanogr.*, **28**, 944–970.
- Lenderink, G., and H. Haarsma, 1994: Variability and multiple equilibria of the thermohaline circulation associated with deep-water formation. *J. Phys. Oceanogr.*, **24**, 1480–1493.
- Madec, G., M. Lott, and M. Crepon, 1996: Large-scale preconditioning of deep-water formation in the northwestern Mediterranean Sea. *J. Phys. Oceanogr.*, **26**, 1393–1408.
- Marotzke, J., 1991: Influence of convective adjustment on the stability of the thermohaline circulation. *J. Phys. Oceanogr.*, **21**, 903–907.
- Marshall, J., A. Adcroft, C. Hill, L. Perelman, and C. Heisey, 1997a: A finite-volume, incompressible Navier–Stokes model for studies of the ocean on parallel computers. *J. Geophys. Res.*, **102**, 5753–5766.
- , C. Hill, L. Perelman, and A. Adcroft, 1997b: Hydrostatic, quasi-hydrostatic, and non-hydrostatic ocean modelling. *J. Geophys. Res.*, **102**, 5733–5752.
- Maxworthy, T., and S. Narimousa, 1994: Unsteady turbulent convection into a homogeneous, rotating fluid, with oceanographic applications. *J. Phys. Oceanogr.*, **24**, 865–887.
- Pedlosky, J., 1985: The instability of a continuous heton cloud. *J. Atmos. Sci.*, **42**, 1477–1486.
- Rahmstorf, S., 1995: Multiple convection patterns and thermohaline flow in an idealized OGCM. *J. Climate*, **8**, 3028–3039.
- Saunders, P. M., 1973: The instability of a baroclinic vortex. *J. Phys. Oceanogr.*, **3**, 61–65.

- Schott, F., and K. D. Leaman, 1991: Observations with moored acoustic doppler current profilers in the convection regime in the Golfe du Lion. *J. Phys. Oceanogr.*, **21**, 558–574.
- , M. Visbeck, and J. Fischer, 1993: Observations of vertical currents and convection in the central Greenland Sea during the winter of 1988–1989. *J. Geophys. Res.*, **98**, 14 401–14 421.
- Send, U., and J. Marshall, 1995: Integral effects of deep convection. *J. Phys. Oceanogr.*, **25**, 855–872.
- Stull, R. B., 1988: *An Introduction to Boundary Layer Meteorology*. Kluwer Academic, 666 pp.
- Vellinga, M., 1998: Multiple equilibria of the thermohaline circulation as a side effect of convective adjustment. *J. Phys. Oceanogr.*, **28**, 305–319.
- Visbeck, M. J., J. Marshall, and H. Jones, 1996: Dynamics of isolated convective regions in the oceans. *J. Phys. Oceanogr.*, **26**, 1721–1734.
- Yin, F. L., and E. S. Sarachik, 1994: An efficient convective adjustment scheme for ocean general circulation models. *J. Phys. Oceanogr.*, **24**, 1425–1430.